Validation of Repetitive Volcanoseismic Signals in Aso Volcano, Japan With Distant Stations: Implications of Source Characterization and Remote Sensing in Uninstrumented Volcanoes

Jieming Niu[1,2] and **Teh-Ru Alex Song[2]**

[1]Key Laboratory of Earth and Planetary Physics, Institute of Geology and Geophysics, Chinese Academy of Sciences, Beijing, China, [2]Seismological Laboratory, Department of Earth Sciences, University College London, London, UK

Abstract Repetitive volcanoseismic signals, including very-long-period signals (VLP) and long-period signals (LP), provide a unique probe of fluid transport processes inside magmatic-plumbing system. While syneruptive signals are often detected and analyzed with regional or/and global seismic networks to retrieve eruption location and mechanism, repetitive noneruptive volcanoseismic signals are generally small, and they are typically detected with in situ stations near the volcanic edifices. Here, we show that repetitive VLP and synchronous deformation events in Aso volcano, Japan, can be detected in the high (15–30 s) and low (50–100 s) VLP bands, respectively, at seismic stations located ∼30–1,000 km away from their sources. Changes in the polarities, phases, and amplitudes of VLP and synchronous deformation events observed at the in situ stations can be verified by the seismic waves in the two VLP bands, respectively, at distant stations up to 150 km. Forward modeling of the amplitude decay in the two VLP bands against epicentral distance corroborates the source locations previously determined by the in situ data, whereas the joint data analysis of in situ and distant stations at high VLP band suggests the presence of single-force component (i.e., force/moment ratio of 10^{-4} m^{-1}) in the source of VLPs. We advocate that not only can systematic data mining against established global and regional seismic networks potentially expand the detection capability of repetitive volcanoseismic signals backward in time when in situ observations were unavailable, but it could also substantially improve the detection and monitoring capacity in otherwise uninstrumented volcanoes, complementary to remote sensing of ground deformation.

Plain Language Summary Seismic signals emitted from volcanic regions carry invaluable information on the transport of magma or/and hydrothermal fluid beneath the volcanic edifice. During explosive eruptions, seismic signal can be detected and analyzed using regional or global seismic networks. On the other hand, during the intereruption interval, repetitive volcanoseismic signals directly linked to fluid transport in the magma plumbing system rely on in situ seismic stations near the volcano edifice. Using repetitive seismic signals from one of the most active volcanoes in Aso as an example, we demonstrate that synchronous seismic signals emitted from a shallow crack-like conduit and a deep chamber roof can be detected at seismic stations even hundreds of kilometers away from their sources. The inclusion of data at distant stations from established global and regional seismic networks improves source characterization, expands the detection capability of repetitive volcanoseismic signals backward in time and increases the monitoring capacity of uninstrumented volcanoes.

1. Introduction

Monitoring active volcanoes plays an essential role in volcanology and hazard mitigation. The information underpinned by ground deformation, volcano seismic signals, volcano degassing, infrasound, and other multidisciplinary observations forms the basis of volcano monitoring (e.g., Fee & Matoza, 2013; Pallister & McNutt, 2015; Pritchard et al., 2019; Sparks et al., 2012) which helps understand the dynamics of the transcrustal magmatic system (e.g., Cashman et al., 2017; Sparks et al., 2019) and ultimately mitigate volcanic hazard (e.g., Bell et al., 2016; Pallister & McNutt, 2015; Tilling, 2008). Volcanoseismic signals, such as volcanotectonic earthquakes, long-period signals, very-long-period signals, continuous tremors, and explosion earthquakes provide invaluable insights to underlying processes governing the fluid transport inside the magmatic-plumbing

Software: Jieming Niu
Supervision: Teh-Ru Alex Song
Validation: Jieming Niu, Teh-Ru Alex Song
Visualization: Jieming Niu
Writing – original draft: Jieming Niu
Writing – review & editing: Teh-Ru Alex Song

system and impending eruptions (e.g., Chouet & Matoza, 2013; Kawakatsu & Yamamoto, 2007; Nishimura & Iguchi, 2011).

Seismic signals excited by volcanic eruptions can be recorded at large epicentral distances. For example, seismic body/surface waves excited by the 1980 Mount St. Helens eruption have been well captured by the Global Digital Seismographic Network locating up to ~15,000 km away from the volcano (Kanamori et al., 1984; Kanamori & Given, 1982). Syneruptive seismic signals recorded by distant stations have been interrogated to understand the eruption mechanisms associated with subaerial volcanoes (e.g., Burger & Langston, 1985; Cruz-Atienza et al., 2001; Duputel & Rivera, 2019; Kanamori & Mori, 1992; Minson et al., 2007; Prejean & Brodsky, 2011; Ruppert et al., 2011; Takeo et al., 1990) and a few submarine volcanoes (e.g., Cesca et al., 2020; Kanamori et al., 1993; Shuler et al., 2013; Tepp et al., 2020; Ye et al., 2020). Large volcanic eruptions can also induce ground resonances at normal-mode frequencies and they are analyzed to explore the coupling between the solid earth and the atmosphere (e.g., Kanamori et al., 1994; Nishida et al., 2000; Watada & Kanamori, 2010; Widmer & Zürn, 1992). More recently, the detection and characterization of seismic-acoustic and broadband infrasound signals also provide additional constraints on the process of explosive volcanic activities (e.g., Fee et al., 2017; Matoza et al., 2018, 2019).

Volcanoseismic signals inside a magmatic or hydrothermal system, including very-long-period signals (VLP, 2–100 s), long-period signal (LP, 0.2–2 s), or episodic deformation events, can potentially provide invaluable constraints on the transport processes of fluids (magma or/and gas) leading to the eruption (e.g., Bell et al., 2018; Chouet, 1996; Chouet et al., 1994; Chouet & Matoza, 2013; Crozier & Karlstrom, 2021; Cruz & Chouet, 1997; Cusano et al., 2015; Dawson & Chouet, 2014; Frank et al., 2018; Jolly et al., 2017; Lokmer et al., 2008; Lyons & Waite, 2011; Matoza & Chouet, 2010; Miller et al., 1998; Niu & Song, 2020, 2021; Ohminato et al., 1998; Rowe et al., 1998; Varley et al., 2010; Waite et al., 2013; Woods et al., 2018; Yamamoto et al., 2002). Typically, they are monitored and characterized by in situ stations near the edifice (i.e., <10 km). While such repetitive volcanoseismic signals are typically small and rarely detected with distant stations (e.g., >10–100 km, Kawano et al., 2020), the use of distant stations in characterizing their source properties and inferring magmatic/hydrothermal processes should not be overlooked in remote, uninstrumented volcanoes that are lack of dedicated local instrumentation and monitoring. The obvious issue is whether it is feasible to observe such weak but repetitive signals and examine their source properties (e.g., location, mechanism).

Unlike crustal earthquakes, where double-couple moment tensor source mechanisms are used to characterize shear faulting (Aki & Richards, 2002), volcanic eruptions and volcanoseismic signals such as explosion earthquakes, VLP and LP often involve volumetric moment tensor component or/and single-force component (e.g., Chouet & Matoza, 2013; Kanamori et al., 1984; Kanamori & Given, 1982; Nishimura & Iguchi, 2011). These source components are often associated with the volumetric change of magma reservoirs and the reaction force responding to the migration of magma or/and magmatic-hydrothermal fluids, respectively (e.g., Chouet & Matoza, 2013; Nishimura & Iguchi, 2011).

However, it is not trivial to constrain the single-force component in the source of volcanoseismic signals with in situ data alone. In particular, when the force/moment ratio is much less than 10^{-3} m^{-1}, the response from a single-force source is much weaker than that from an isotropic source (e.g., Chouet et al., 2003; Uhira & Takeo, 1994). Furthermore, when the seismic wavelength is long compared with the source depth, it has been argued that the source equivalence between a vertical single-force and horizontal tensile crack (e.g., Day & McLaughlin, 1991) could make it difficult to resolve the single-force source component in volcanic settings (e.g., Dawson & Chouet, 2019).

The main aim of this paper is to analyze data at distant stations and validate the source properties of repetitive VLP and synchronous deformation events previously determined by in situ data near the active crater (i.e., <10 km) (e.g., Legrand et al., 2000; Niu & Song, 2021). Specifically, we analyze data recorded by the F-net of Japan up to ~100–1,000 km away from these sources. We elaborate several steps to evaluate the prospect of source detection and source mechanism appraisal. After accounting for previous observations of volcanoseismic signals at Aso volcano in Section 2, as detailed in Sections 3 and 4, we first use the event catalog readily available from Niu and Song (2020, 2021) to tease out observations of VLP and deformation events at the distant stations (i.e., >30 km). In Section 5, observations at the distant stations away from the crater help appraise source locations/mechanisms previously determined by in situ data near the crater. In particular, distant stations can be
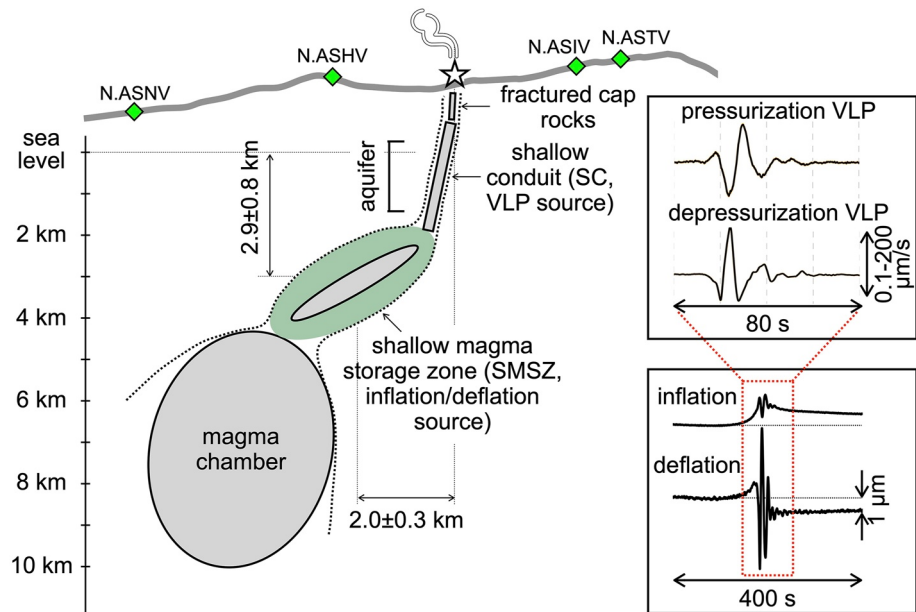
Figure 1. An east-west cross section displaying the magma plumbing system beneath Aso volcano, Japan. The shallow crack-like conduit (SC) marks the source region of pressurization (depressurization) very-long-period signals (VLP). The shallow magma storage zone (SMSZ) indicates the source location of the deformation (inflation or deflation) event. The lower inset shows the representative broadband waveform stacks of inflation and deflation events, whereas the upper inset zooms in the stacked waveforms to display pressurization (depressurization) VLP synchronized with the inflation (deflation) event.

advantageous in constraining single-force component of the source, leading to the identification of single-force component associated with repetitive VLPs at Aso volcano. Finally, in Section 6, we briefly discuss the potentials of remote monitoring and source characterization of volcanoseismic signals in less-instrumented and uninstrumented volcanoes.

2. Repetitive VLP and Deformation Event Beneath Aso Volcano

2.1. Repetitive VLP in Aso Volcano

Since the first discovery by Sassa (1935), persistent VLP in Aso has been reported for almost a century (Kaneshima et al., 1996; Kawakatsu et al., 2000; Kubotera, 1974; Niu & Song, 2020; Sakaguchi et al., 2008; Sassa, 1936; Yamamoto et al., 1999). Modern broadband seismometers near the active Naka-dake First crater help characterize VLP as an event-like signal with a dominant period of ~15 s and a duration of ~60 s (Kaneshima et al., 1996; Kawakatsu et al., 2000). The source of VLP is dominated by a volumetric source located at ~200 m southwest of the Naka-dake First crater in a shallow crack-like conduit (SC) near the sea level (Legrand et al., 2000; Yamamoto et al., 1999, Figure 1), corresponding to a region of low seismic velocity (Huang et al., 2018) and modestly high conductivity (Hase et al., 2005; Hata et al., 2016, 2018; Kanda et al., 2019), most likely a hydrothermal reservoir.

Several VLP families have also been detected with diverse initial polarity and resonance period in the same proximity and their activities appear to vary systematically with surface volcanic activities (Niu & Song, 2020). Typical VLP waveform starts with a negative polarity and it is interpreted as a result of a rapid release of the fluid-gas mixture through fracture (depressurization VLP, Figure 1) (Kawakatsu et al., 2000; Niu & Song, 2020). During the phreatic eruption in 1993–1994, VLPs with a positive initial polarity were occasionally recognized and they are regarded as a result of rapid pressurization due to vaporization induced by magmatic heat and supply of hot liquid/gas from below (pressurization VLP, Figure 1) (Kaneshima et al., 1996; Kawakatsu et al., 2000). A substantial number of these pressurization VLPs were later identified before the 2014 Strombolian eruption and the 2015/2016 phreatomagmatic eruption (Niu & Song, 2020).
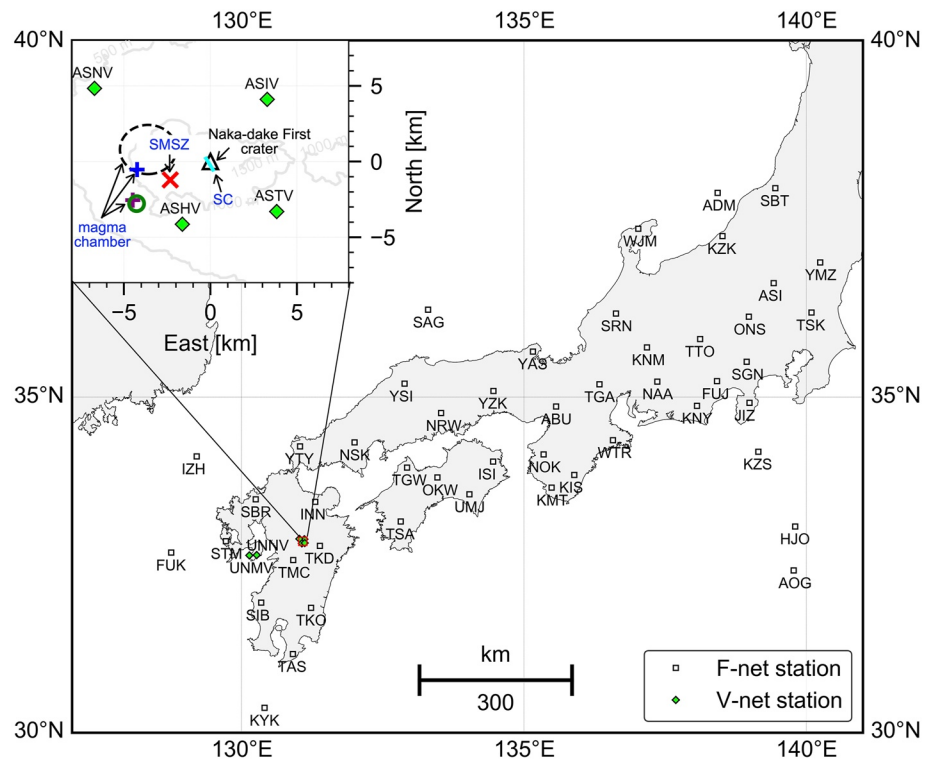
Figure 2. Maps of in situ and distant broadband seismic stations around Aso volcano. The map of broadband seismic stations operated by the F-net (open square) and V-net (green diamond). The in situ V-net stations near the Naka-data First crater of Aso volcano are highlighted in the inset. The locations of the magma chamber inferred from geodetic data are shown by the purple cross and green circle (Sudo et al., 2006) and blue circle (Ohkura et al., 2009). The low seismic velocity zone is indicated by the dashed circle (Sudo & Kong, 2001). Shallow crack-like conduit (SC) is marked by the blue bar.

2.2. Repetitive Deformation Events in Aso Volcano

Most recently, deformation events synchronous with VLP have been documented by Niu and Song (2021) using data from the fundamental volcano observation network (Tanada et al., 2017), or the V-net. Observations from in situ V-net stations show that these events typically precede VLP by ~50 s and conclude seconds after. Displacement and tilt amplitude ratios among different stations or different components show considerable coherency among events at an ultralong period of 50–250 s, suggesting a relatively stationary source. High-quality broadband waveform stacks reveal clear static offset in the V-net stations, where a positive (negative) displacement and eastward (westward) tilt observed at the station ASHV corresponds to inflation (deflation) events (Figure 1). These inflation or deflation events are located ~2 km southwest of the Naka-dake First crater and ~3 km below sea level and they are characterized by a major volumetric component (~80%) and a minor normal-fault component (~20%) (Niu & Song, 2021) (Figure 1). Together with petrological evidence, Niu and Song (2021) suggested that these inflation/deflation events likely represent episodic transport of discrete magma batches from the volatile-poor silicic magma chamber toward a shallow magma storage zone (SMSZ), a preeruptive pool with mixed magma. In the following sections, the sources of VLP and synchronous deformation events are referred as SC and SMSZ, respectively, hereafter.

3. Data

In this study, we include 47 broadband seismic stations operated by National Research Institute for Earth Science and Disaster Resilience (NIED) F-net (Okada et al., 2004) and six broadband seismic stations operated by NIED V-net (Tanada et al., 2017, Figure 2). The distances between the F-net stations and the Naka-dake First crater range from ~30 to ~1,000 km. Four V-net stations are located with a distance of <10 km to the crater (Figure 2, inset) and they were previously used to identify the diversity of the VLP (Niu & Song, 2020) and the presence

of the deformation events (Niu & Song, 2021). Two additional V-net stations are in Unzen volcano, and they are ~70 km from the Naka-dake First crater. We consider stations located within the edifice, less than 10 km from the Naka-dake First crater, as the in situ stations (Figure 2, inset), whereas stations located outside the edifice, more than 10 km away from the Naka-dake First crater, are regarded as the distant stations.

The F-net stations are equipped with Streckeisen STS-2 broadband sensor with a nominal natural period of ~120 s (Okada et al., 2004; see also https://www.fnet.bosai.go.jp/st_info/response.php?LANG=en) and the V-net stations are equipped with Nanometrics Trillium 240 broadband sensor with a nominal natural period of ~250 s (Tanada et al., 2017). The gain of the V-net and F-net stations is calibrated within ~3% and the sensor misorientation in the horizontal components is also minimum and corrected (Niu & Song, 2020).

The VLP catalog in 2011–2016 was constructed by Niu and Song (2020) using two three-component broadband (ASHV and ASIV, a natural period of ~250 s, ~3 km apart from the VLP source) from V-net and a three-component borehole short-period seismometers (a natural period of 1 s, ~0.5 km apart from the VLP source) from Japan Meteorological Agency. The pressurization and depressurization VLP families were identified by a continuous wavelet transform technique (Niu & Song, 2020). The matched-filter technique was then applied to construct the VLP catalog with a nominal false-pick rate below 0.1%, which includes ~0.2 million events in 2011–2016 (Niu & Song, 2020).

We collect seismic data at the F-net and V-net stations against all detected VLP events in 2011–2016 (Niu & Song, 2020) and each seismogram includes a duration of 20 min, starting at ~280 s before the onset time of VLP. After removing the background trend and the mean, we remove the instrumental response in the frequency band of 0.001–10 Hz and obtain velocity waveforms. As noted earlier, VLP has a dominant period of ~15 s, whereas the deformation event can be recognized at the period of 50–250 s. Therefore, in the subsequent analysis, we filter the velocity data in the frequency bands of 0.03–0.07 Hz and 0.01–0.02 Hz and seek the energy associated with the VLP and the deformation event, respectively. Hereafter, we refer to the signals at 0.03–0.07 Hz as the high VLP band signal and those at 0.01–0.02 Hz as the low VLP band signal, respectively. Following observations in earlier studies, we first focus the analysis on the vertical component.

4. Observations of VLPs and Synchronous Deformation Events at the V-Net and F-Net

Here we systematically highlight observations of VLP and synchronous deformation events against single-event data (Section 4.1), multimonth global waveform stacks (Sections 4.2 and 4.3), and monthly waveform stacks (Section 4.3). In Sections 4.2 and 4.3, we examine systematics during the periods of volcanic unrest in November 2011 to August 2014 and Strombolian eruption in October 2014 to May 2015. These examples aim to demonstrate that the diverse nature of VLP and synchronous deformation events observed in situ (e.g., V-net) can be readily validated by observations at distant stations (e.g., F-net).

4.1. High/Low VLP Band Record Sections From the Two Largest VLPs and Synchronous Deformation Events

Figure 3 displays high-quality record sections in the high and low VLP bands from the two largest events in the catalog and these record sections are organized against the locations of the SC and the SMSZ, respectively. The record section in the high VLP band demonstrates that the vertical, radial, and transverse energy from the two VLPs can be observed up to ~1,000 km or more with an apparent velocity of ~3.2 km/s (Figures 3a–3c) and it does not show significant change against the epicentral distance. Similarly, we can also identify consistent energy in the low VLP band up to ~1,000 km in the vertical component (Figure 3d), admittedly with a lower signal-to-noise ratio beyond ~500 km. This observation in the high VLP band is consistent with earlier studies by Hashida (1990) and Kawakastu et al. (1994, 2000).

In general, the energy in the low VLP band is a factor of ~20 smaller the one in the high VLP band. As indicated in Figure 3a, the amplitude of high VLP band energy drops from the four V-net stations at ~5 km distance (blue traces in Figure 3a) to the nearest F-net stations at ~25 km distance (i.e., TKD, TMC) by about a factor of 10. In contrast, the amplitude of low VLP band energy drops from the four V-net stations (blue traces in Figure 3d)
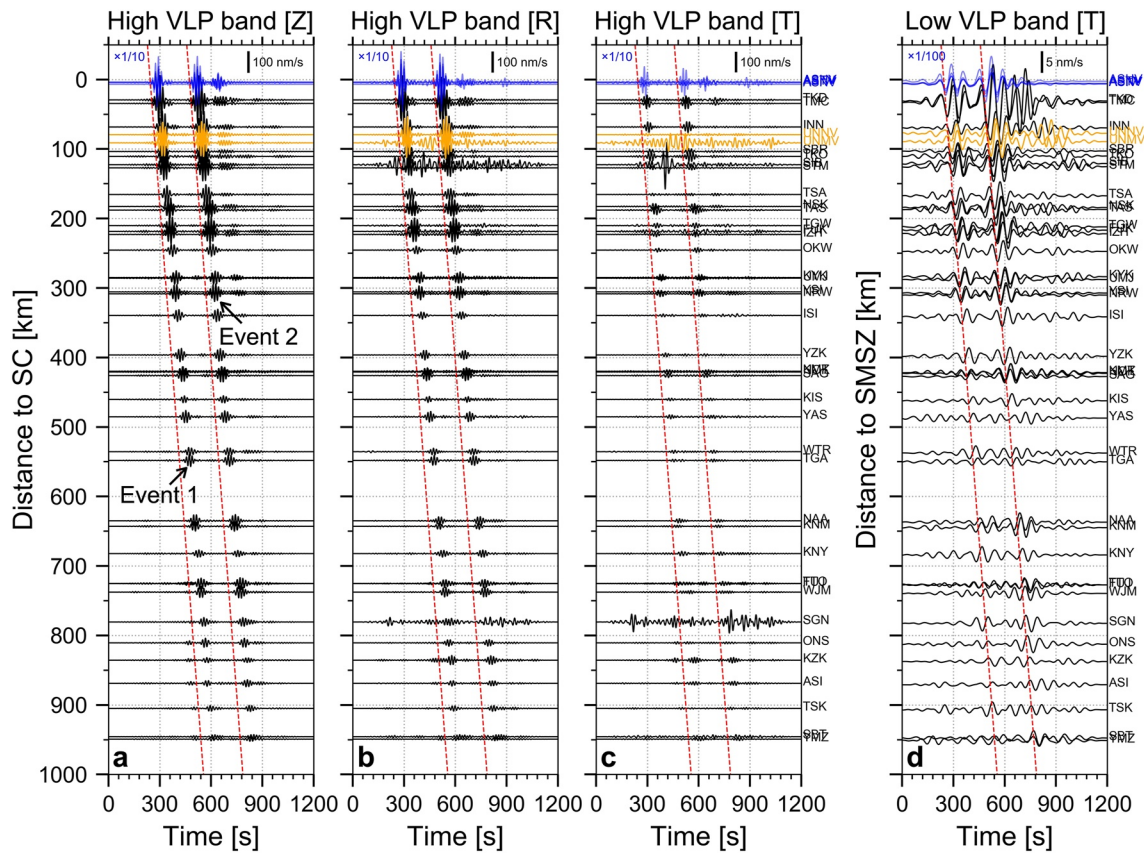
Figure 3. Waveform record sections in the high/low very-long-period signals (VLP) bands from two large events before the 8 October 2016, phreatomagmatic eruption. (a–c) The record sections of high VLP band velocity seismograms (0.03–0.07 Hz) in the vertical (Z), radial (R), and transverse (T) components, including waveforms recorded at the V-net (blue and yellow traces) and F-net (black traces) stations, respectively. The seismograms with a low signal-to-noise ratio are excluded. The starting time of the seismograms is 2016-10-08T01:36:26 (JST). The seismograms recorded at the four in situ V-net stations (blue) are downscaled by a factor of 10 for the presentation. The seismograms recorded around the Unzen volcano are in yellow. The red dashed lines mark the apparent velocity of 3.2 km/s. The first and second events are marked as Event 1 and Event 2, respectively. (d) Same as (a), except showing the vertical-component record section of low VLP band velocity seismograms (0.01–0.02 Hz). The in situ recordings at V-net (blue traces) are downscaled by a factor of 100 for the presentation.

to the nearest F-net stations (i.e., TKD, TMC) by about a factor of 100. As detailed in Section 5, such a large difference is unlikely a result of attenuation, but due to differences in the source property (i.e., source depth) between the SC and the SMSZ.

4.2. Global Waveform Stacks During Volcanic Unrest and the Strombolian Eruption

Since VLPs and synchronous deformation events are repetitive, one should demonstrate that the energy observed from single-event record sections in Section 4.1 can be duplicated. As detailed in Niu and Song (2021), the pressurization VLP and the inflation events are prominent during the volcanic unrest between November 2011 and August 2014, whereas the depressurization VLP and the deflation events are dominant during the Strombolian eruption between October 2014 and May 2015. By utilizing the timing of VLP detected from in situ data (Niu & Song, 2020), we construct global waveform stacks from inflation events in the period of the volcanic unrest and deflation events during Strombolian eruption, respectively. We note that events during the malfunction of F-net stations (https://www.fnet.bosai.go.jp/st_info/station_dat.php?LANG=en) are excluded and, as a result, 665 of 671 inflation events and 714 of 957 deflation events are used to construct the global inflation and deflation waveform stacks, respectively.

To construct the waveform stacks at each station, high/low VLP band waveforms are normalized against their peak velocities before stacking and the median of the peak velocities is multiplied against the waveform stacks
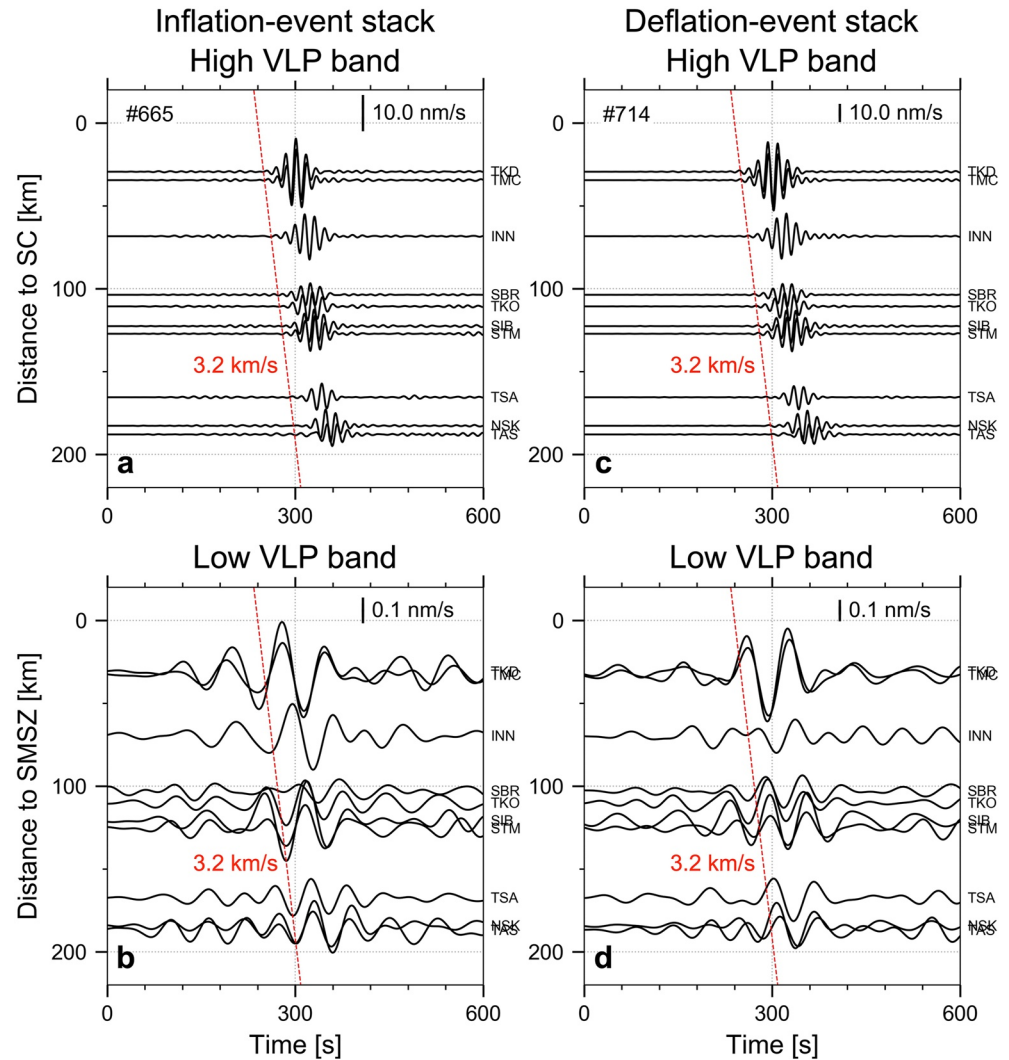
Figure 4. Record sections of global inflation/deflation event waveform stacks. (a) and (b) display high very-long-period signals (VLP) band (0.03–0.07 Hz) and low VLP band (0.01–0.02 Hz) record sections of the global inflation event waveform stacks (November 2011-August 2014) at the F-net stations, respectively. (c) and (d), same as (a) and (b), except displaying the record sections of the global deflation events waveform stacks (October 2014-May 2015). The red dashed lines mark the apparent velocity of 3.2 km/s. The complete record sections up to 1,000 km distance can be referred to Figure S1 in Supporting Information S1.

to recover their amplitudes. Figures 4a and 4b display the high/low VLP band record sections from global inflation waveform stacks. While the energy associated with pressurization VLPs can be easily identified in the high VLP band up to 1,000 km, the energy associated with inflation events in the low VLP band is weak with a lower signal-to-noise ratio. This is not surprising since the amplitude of the deformation events is generally two orders of magnitude smaller than the two largest events discussed in Section 4.1 (see also Niu & Song, 2021). As the amplitudes of low VLP band waveform stacks are ~100 times smaller than that of high VLP band waveform stacks, their signal-to-noise ratios remain relatively poor beyond ~200–300 km (Figures S1a and S1b in Supporting Information S1). Similarly, when examining the record sections from global deflation waveform stacks (Figures 4c and 4d; Figures S1c and S1d in Supporting Information S1), we can also identify the energy associated with VLPs in the high VLP band record section (Figure 4c and Figure S1c in Supporting Information S1) and observe weak, but consistent energy associated with deflation events in the low VLP band record section (Figure 4d and Figure S1d in Supporting Information S1).
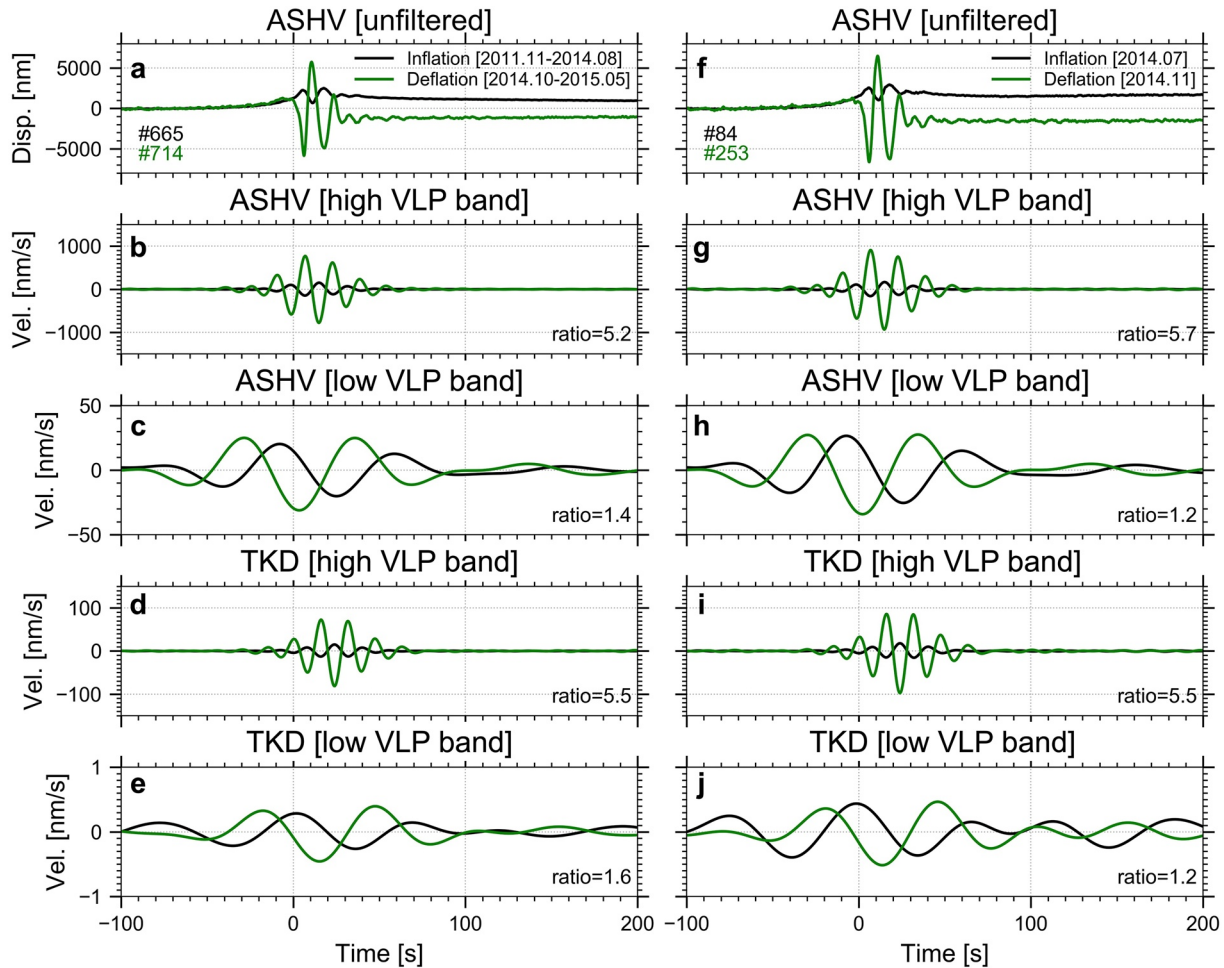
Figure 5. Polarity, phase, and amplitude of short/long-period waveform stacks at the in situ and distant stations. (a–c) Broadband displacement, high very-long-period signals (VLP) band (0.03–0.07 Hz) and low VLP band (0.01–0.02 Hz) velocity seismograms of the global inflation/deflation waveform stacks at the in situ station ASHV, respectively. (d, e), same as (b, c), except displaying high VLP band (0.03–0.07 Hz) and low VLP band (0.01–0.02 Hz) waveform stacks at the distant F-net station TKD, respectively. (f–j), Same as (a–e), except displaying the monthly inflation (July 2014) and deflation (November 2014) waveform stacks. (a–e) and (f–j) Demonstrate the consistency between observations at in situ and distant stations.

4.3. Diverse VLPs and Synchronous Deformation Events During Volcanic Unrest and Strombolian Eruption

In Sections 4.1 and 4.2, we have shown that the energy associated with repetitive VLPs and synchronous deformation events can be robustly detected at distant stations up to ∼200–1,000 km. While changes in the polarities and amplitudes of VLPs and synchronous deformation events against surface volcanic activities can be identified at in situ stations, here we demonstrate that these systematic differences can be readily observed at the distant stations (Figure 5). Figures 5a–5c show the unfiltered displacement, high VLP band velocity, and low VLP band velocity global waveform stacks at the in situ station ASHV. The unfiltered displacement stacks are obtained by integrating unfiltered velocity waveform stacks and the removal of nonlinear drift by a fourth-order polynomial function (Niu & Song, 2021; Zhu, 2003) (Figure S2 in Supporting Information S1).

As shown in Figures 5a and 5b, the amplitude of VLPs in the deflation stacks is ∼3 times higher than that in the inflation stacks. On the other hand, the amplitudes of static offset and low VLP band energy in the inflation and deflation waveform stacks are very similar (Figures 5a and 5c). One can easily recognize that the polarities of VLP and synchronous deformation events are opposite between the inflation waveform stacks and the deflation waveform stacks (Figures 5a–5c). Furthermore, we can identify a phase delay between the global inflation and deflation stacks in the low VLP band (Figure 5c). As illustrated in Figures 5d and 5e, observations made at the in situ station ASHV can be readily confirmed by the high/low VLP band waveform stacks at the F-net station TKD

Table 1
Locations and Source Mechanisms of the SC and SMSZ Used in the Synthetic Calculation

Source	Latitude (°)	Longitude (°)	Depth (km)	M_{xx}	M_{yy}	M_{zz}	M_{xy}	M_{xz}	M_{yz}	Reference
SC	32.8832	131.0830	(0.2), 1–8	0.690	1.000	0.763	0.090	0.056	−0.040	Legrand et al. (2000)
SMSZ	32.8758	131.0642	0.2, 1–8, (3)	0.863	1.000	0.625	0.077	0.066	0.102	Niu and Song (2021)

Note. The moment tensor is normalized and defined in x=North, y=East and z=Down. The depth in the parentheses indicates the source depth previously derived from the in-situ data (see reference).

(i.e., ∼30 km from the sources). Finally, we examine high-quality monthly inflation waveform stacks of July 2014 and monthly deflation waveform stacks of November 2014 (Figures 5f–5j). It is evident that observations made previously against global waveform stacks can be replicated by high-quality monthly waveform stacks.

5. Validating Source Properties of VLP and Synchronous Deformation Events in Aso With Data at Distant Stations

We have shown that the persistence and diversity of VLPs and synchronous deformation events can be validated by recordings at the distant stations. As noted by Niu and Song (2021) and discussed earlier, the source of VLPs (i.e., SC) and synchronous deformation events (i.e., SMSZ) are spatially separated by about 3 km. While the depth of the SC is close to sea level, or 1.5 km below the crater bottom (Kawakatsu et al., 2000; Legrand et al., 2000; Niu & Song, 2020; Yamamoto et al., 1999), the depth of the SMSZ is ∼3 km below sea level and ∼2 km west of the Naka-dake First crater (Niu & Song, 2021, see also Figure 1). In this instance, one would expect that the amplitude decay pattern against the epicentral distance, dictated by the source depth (Aki & Richards, 2002; Legrand et al., 2000; Niu & Song, 2021), would differ substantially among high VLP band velocity, low VLP band velocity, and static displacement. On the other hand, both VLPs and synchronous deformation events are dominated by a volumetric component (Legrand et al., 2000; Niu & Song, 2021; Yamamoto et al., 1999). Here we also explore how the data at distant station can facilitate validation of these source mechanisms previously derived from in situ data.

5.1. Validating Source Depths of VLP and Deformation Event

To cross-validate their source depths, we measure the amplitudes of the high/low VLP band velocity and static displacement offset and compare them against synthetics. To calibrate the receiver effect on the velocity amplitude at each station, we compare the peak velocities of high/low VLP band Rayleigh waves from distant great earthquakes against those recorded at the reference station (i.e., ASHV). Specifically, we obtain the averaged amplitude of high VLP band (or low VLP band) Rayleigh waves from selected teleseismic events in 2011–2016, including 24 earthquakes with Mw ≥ 7, the source depth of ≤50 km, and the epicentral distance of ≥30°. The averaged amplitude is corrected for the geometric spreading and normalized against the averaged Rayleigh wave amplitude at the reference station ASHV to obtain the station specific amplitude correction factor (Figure S3 in Supporting Information S1).

Synthetic seismograms are calculated by the F-K package (Zhu & Rivera, 2002) against the 1D global reference velocity model IASP91 (Kennett et al., 1995) with attenuation structure adapted from Preliminary Reference Earth Model (PREM, Dziewonski & Anderson, 1981). Static displacement offset is calculated for a point source embedded in a homogeneous half-space (Okada, 1992), where $v_P = 1,500$ m/s, $v_S = 800$ m/s, and $\rho = 1,700$ kg/m³ (Legrand et al., 2000; Niu & Song, 2021). The moment tensors of the SC (Legrand et al., 2000) and a triangle source-time function of 8 s are used to compute synthetics against high VLP band observations (Table 1). On the other hand, the moment tensor of the SMSZ (Niu & Song, 2021) and a triangle source-time function of 60 s are used to compute synthetics against long-period observations. Note that the durations of these source-time functions are consistent with the dominant period of VLP and the rise time of inflation/deflation events, respectively. However, these specific choices do not noticeably change the rate of amplitude decay against epicentral distance.

We note that, in these calculations, the SC and SMSZ are fixed at the geographical locations derived previously from Legrand et al. (2000) and Niu and Song (2021), respectively. However, to test the validity of the source
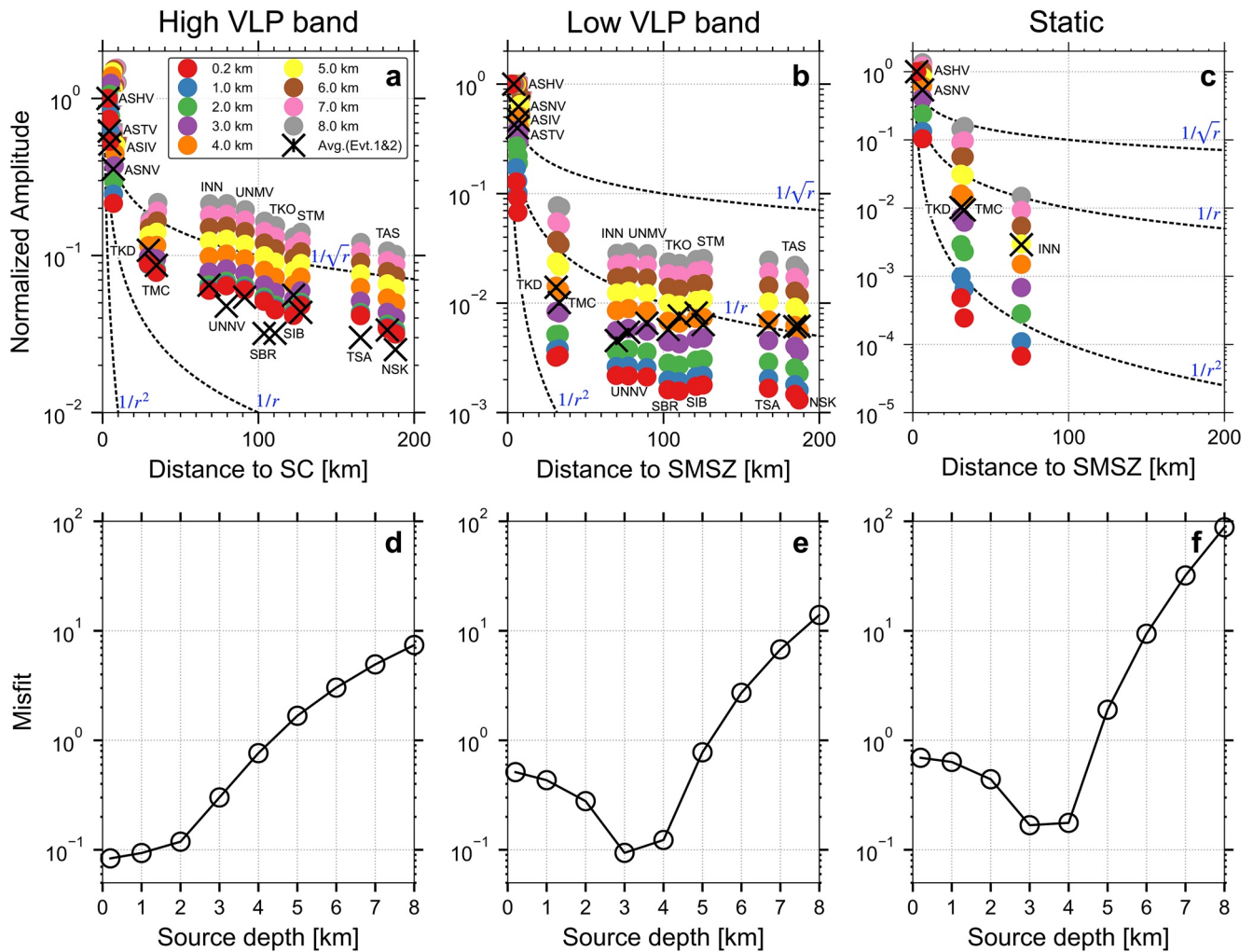
Figure 6. Forward modeling the amplitude versus distance decay trend against the high/low very-long-period signals (VLP) band waveforms and static displacements at Event 1 and Event 2. (a) Comparing peak-to-peak velocity between observations (crosses) and synthetics (solid circles) in the high VLP band (0.03–0.07 Hz). Synthetics are color-coded against the source depths. The observed amplitudes are the average of Event 1 and Event 2, whereas the observed and synthetic amplitudes are normalized by the amplitude at the station ASHV. The epicentral distance is computed against the location of the shallow crack-like conduit (SC). (b) and (c), same as (a), except for the low VLP band velocity (0.01–0.02 Hz) and static displacement, respectively, and the epicentral distance is computed against the shallow magma storage zone (SMSZ). In (c), robust observations of static displacement can be obtained at the two in situ stations (ASHV, ASNV) and the distant stations TKD, TMC, and INN. The amplitude-distance decay trends following $1/\sqrt{r}$, $1/r$, and $1/r^2$ are marked by dashed lines, where r is the hypocentral distance for a surface source. (d–f) The misfits between the normalized synthetic and observed amplitudes against the source depths in the high VLP band velocity (0.03–0.07 Hz), the low VLP band velocity (0.01–0.02 Hz), and static displacement, respectively.

depths of the SC (i.e., ~0.2 km below sea level) and the SMSZ (i.e., ~3 km below sea level) obtained in previous studies (Legrand et al., 2000; Niu & Song, 2021; Yamamoto et al., 1999), we compute synthetics against the source depths from 0.2 to 8 km below sea level. Considering the effect of topography on surface displacement (Williams & Wadge, 1998), the effective source depth in the calculation is measured against the reference free surface defined by the station elevation, ranging from ~50 to ~900 m above sea level. Table 1 lists the relevant source parameters used in the calculation.

5.1.1. Modeling Amplitude Decay Against Single-Event Waveform Data

Figures 6a–6c compare the observed amplitude decay of the two largest events (crosses) against synthetics (color dots), where all the measurements are normalized against the amplitude at the reference station ASHV. Within ~30 km, the amplitude decay in the low VLP band (Figure 6b) and in the static offset (Figure 6c) is more than ~10 times faster than that in the high VLP band (Figure 6a), consistent with the observations in Figure 3. Notably, the low VLP band amplitude follows more closely to the $1/r^2$ to $1/r$ decay trend, where r is the hypocentral

distance. In contrast, the high VLP band amplitude follows more closely to the $1/r$ to $1/\sqrt{r}$ decay trend. This is not surprising as the amplitude in the near-field and far-field respectively follows the $1/r^2$ and $1/r$ decay trends (Aki & Richards, 2002), and the transition between the near-field and far-field depends on the dominant wavelength. Beyond ∼30–100 km, the amplitude decay is generally close to $1/\sqrt{r}$, as expected for surface waves (Aki & Richards, 2002).

Synthetics illustrate a strong dependence of amplitude decay rate against the source depth (Figures 6a–6c), that is, the amplitude decays at a faster rate against distance when the source is located at a shallower depth. This systematic trend allows us to validate the source depths of SC and SMSZ. We compute the misfit between observed and synthetic amplitudes against quality measurements at distant stations between 10 and 200 km. The misfit is defined by $1/N \sum_{i=1}^{N} (s_i - o_i)^2/o_i^2$, where N is the number of observations, s_i and o_i the normalized synthetic and observed amplitudes at ith station, respectively. Comparisons between observed and synthetic amplitude against in situ data are included for completeness. As shown in Figure 6d, the amplitude decay in the high VLP band is best explained by a source depth of ∼0.2 km below sea level, whereas the amplitude decay in the low VLP band (Figure 6e) and static offset (Figure 6f) is best explained by a source depth of ∼3–4 km below sea level. Collectively, these results validate the source locations and mechanisms of the SC and the SMSZ derived from in situ stations near the edifices (Legrand et al., 2000; Niu & Song, 2021; Yamamoto et al., 1999).
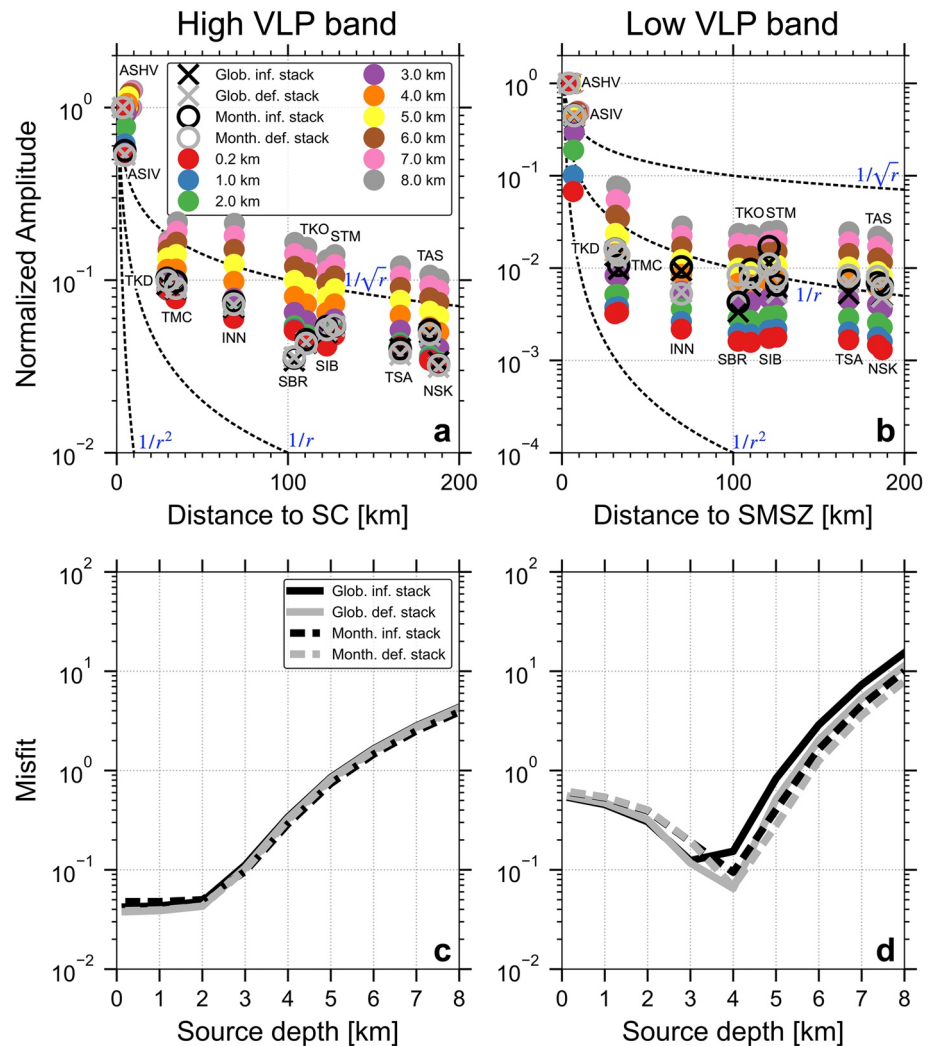
5.1.2. Modeling Amplitude Decay Against the Global and Monthly Waveform Stacks

Following the approach in Section 5.1.1, we illustrate the amplitude decay trends observed from the global and monthly waveforms stacks and compare them against synthetics (Figures 7a and 7b). In general, the amplitudes decay trends from the inflation (black symbols) and deflation (gray symbols) waveform stacks are very similar and there is no apparent difference between the global stacks (crosses) and monthly stacks (open circles). As shown in Figures 7c and 7d, the high VLP band amplitude decay is best explained by a source depth of ∼0.2 km below sea level (Figure 7c), whereas the decay in the low VLP band amplitude (Figure 7d) is best explained by a source depth of ∼3–4 km below sea level. These results again validate the source locations and mechanisms of the SC and the SMSZ derived from stations near the edifices (Legrand et al., 2000; Niu & Song, 2021; Yamamoto et al., 1999), reaffirming the stationary properties of the SC and SMSZ during the 2011–2016 eruption cycle.

5.2. Validating Source Mechanisms of VLP and Deformation Event: The Constraint Against Single-Force Component by Distant Stations

In Section 5.1, we have shown that the source depths of VLP and deformation event previously determined by in situ data are well supported by the data at distant stations. Here we examine the source mechanism of the VLP and deformation events against the single-event data previously discussed in Section 5.1.1 (see also Table 1). Figure 8 compares the observed and synthetic particle motions in the vertical-radial and radial-transverse planes against the in situ station ASHV and several quality distant stations such as TKD, TMC, INN, and STM. Since the transverse component is very noisy in the low VLP band, we only examine the low VLP band particle motion in the vertical-radial plane. As shown in Figure 8a, the low VLP band particle motion associated with the deformation event can be explained reasonably well by the synthetics, suggesting that the source mechanism by Niu and Song (2021) can also reconcile the data in these distant stations.

However, there are some inconsistencies in the high VLP band between the observed and synthetic particle motions associated with the VLP (Figures 8b and 8c). In particular, at the distant stations TMC and TKD (i.e., ∼30 km from the source), the major axes of the observed and synthetic particle motions in the vertical-radial plane tilt in the opposite directions (Figure 8b). At the station TMC, the major axes of the observed and synthetic particle motions in the radial-transverse plane also tilt in the opposite directions (Figure 8c). Previously, Legrand et al. (2000) showed that the source of VLP is predominantly with an isotropic component. They noted that the single-force component was difficult to resolve and perhaps not relevant during phreatic eruptions. As the earlier studies are limited to in situ stations, here we first discuss the advantage offered by the inclusion of distant stations in the source analysis (Section 5.2.1). After elaborating the potential tradeoff between the vertical single-force source and horizontal tensile crack source in Section 5.2.2, we systematically explore if the addition of the single-force component helps reconcile the discrepancy between the data and synthetics in the high VLP band (Section 5.2.3).

Figure 7. Forward modeling the amplitude versus distance decay trend against the high/low very-long-period signals (VLP) band global and monthly inflation and deflation waveform stacks. (a) Comparing peak-to-peak velocity between global stacks (crosses), monthly stacks (circles), and synthetics (solid circles) in the high VLP band (0.03–0.07 Hz). Synthetics are color-coded against the source depths. The observed and synthetic amplitudes are normalized by the amplitude at the station ASHV. The epicentral distance is computed against the location of the shallow crack-like conduit (SC). (b) Same as (a), except for the low VLP band velocity (0.01–0.02 Hz) and the epicentral distance is computed against the shallow magma storage zone (SMSZ). The amplitude-distance decay trends following $1/\sqrt{r}$, $1/r$, and $1/r^2$ are marked by the dashed lines, where r is the hypocentral distance for a surface source. (c) The misfits between the normalized synthetic and observed amplitudes against the source depths in the high VLP band (0.03–0.07 Hz). (d) Same as (c), except in the low VLP band (0.01–0.02 Hz).

5.2.1. Amplitude Ratios Between Isotropic and Single-Force Component at In Situ and Distant Stations

Here we explore the effect of single-force component against data at the in situ and distant stations. Figure 9a shows the peak-to-peak velocity amplitude ratio between a vertical single-force source (i.e., V_{SF}) and an isotropic source (i.e., V_{ISO}) at a fixed force/moment ratio of 10^{-4} m^{-1} against the epicentral distance. Notably, at small epicentral distance where in situ stations are deployed (i.e., <2 km), the amplitude ratio V_{SF}/V_{ISO} is relatively small (i.e., 0.1–0.4). However, as shown in Figure 9a, the amplitude ratio V_{SF}/V_{ISO} increases rapidly with distance and it reaches about ~2–4 beyond 5 (30) km in the vertical (radial) component, suggesting that the velocity from the single-force component is comparably much more prominent than that from the isotropic component at mid-to-large distances (i.e., >~5 km).

This result indicates that the response from a single-force source is comparably much more prominent than that from an isotropic source at distant stations. Early detection of single-force source mechanism in Izu-Oshima with
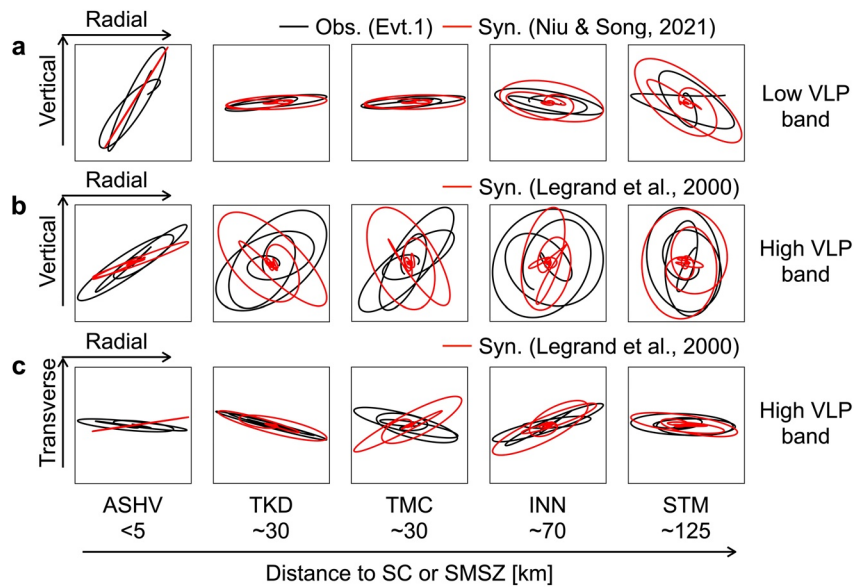
Figure 8. Forward modeling high/low very-long-period signals (VLP) band particle motions. (a) Comparisons of observed low VLP band (0.01–0.02 Hz) particle motions of Event 1 (black) and synthetics (red) in the vertical-radial plane. (b) Comparisons of observed high VLP band (0.03–0.07 Hz) particle motions of Event 1 (black) and synthetics (red) in the vertical-radial plane. (c) Same as (b), except in the radial-transverse plane.

data beyond 30 km (i.e., Ukawa & Ohtake, 1987) perhaps also reflects this important property. This is not surprising since the single-force component decays at a slower rate than the force dipole or force couple component in the near-field (Aki & Richards, 2002; Kanamori & Given, 1982; Ohminato et al., 1998). These results are readily manifested in the particle motions (Figures 9b–9d). As shown in Figures 9b and 9c, the particle motions from a single-force source and an isotropic source differ substantially at the distance of less than 30 km. For a joint source with a force/moment ratio of 10^{-4} m^{-1}, Figure 9d shows that the single-force component alters the particle motion from the isotropic component more substantially at ~5–30 km than that at 1 km.

5.2.2. The Ambiguity Between a Vertical Single-Force Source and a Horizontal Tensile Crack Source?

The result in Section 5.2.1 strongly suggests that data at distant stations can be included to minimize the tradeoff between the isotropic component and the single-force component and improve constraints on the presence/absence of single-force component in the source. However, as noted by Day and McLaughlin (1991), when the seismic wavelength is longer than the source depth, the responses from a vertical single-force and a horizontal tensile crack are equivalent. On the other hand, Fukao (1995, p. 247) pointed out that "….the resultant static displacement is zero according to their single-force model, but non zero according to their fault model, an obvious contradiction to their proposed equivalence between two models…" The discrepancy pointed out by Fukao (1995) suggests that the assertion by Day & McLaughlin (1991) may not be valid in the near-field.

To test this hypothesis, we first compute synthetics from a vertical single-force and a horizontal crack for the source depth of high VLP band signal at 500 m in a homogeneous half-space. Following Equation 16 of Day and McLaughlin (1991), the calculated response from the horizontal tensile crack includes a triangle source-time function of 8 s equivalent to the double-integrated source-time function of the vertical single-force multiplied by the scaling factor v_p^2/h, where v_p is P wave velocity and h is source depth. Figure 10 displays the velocity amplitude ratio between the horizontal tensile crack source (HC) and the single-force source (SF). If the assertion of source equivalence by Day and McLaughlin (1991) were valid, one would expect that the velocity amplitude ratio remains constant against the epicentral distance.

However, as shown in Figure 10a, we find that the velocity amplitude ratios in the high VLP band vary significantly within the range of about 100 km, a distance comparable to signal wavelength in the high VLP band. The amplitude ratios measured in the low VLP band also varies significantly within the range of about 150 km (Figure 10b). These observations support the hypothesis that the source equivalence asserted by Day and
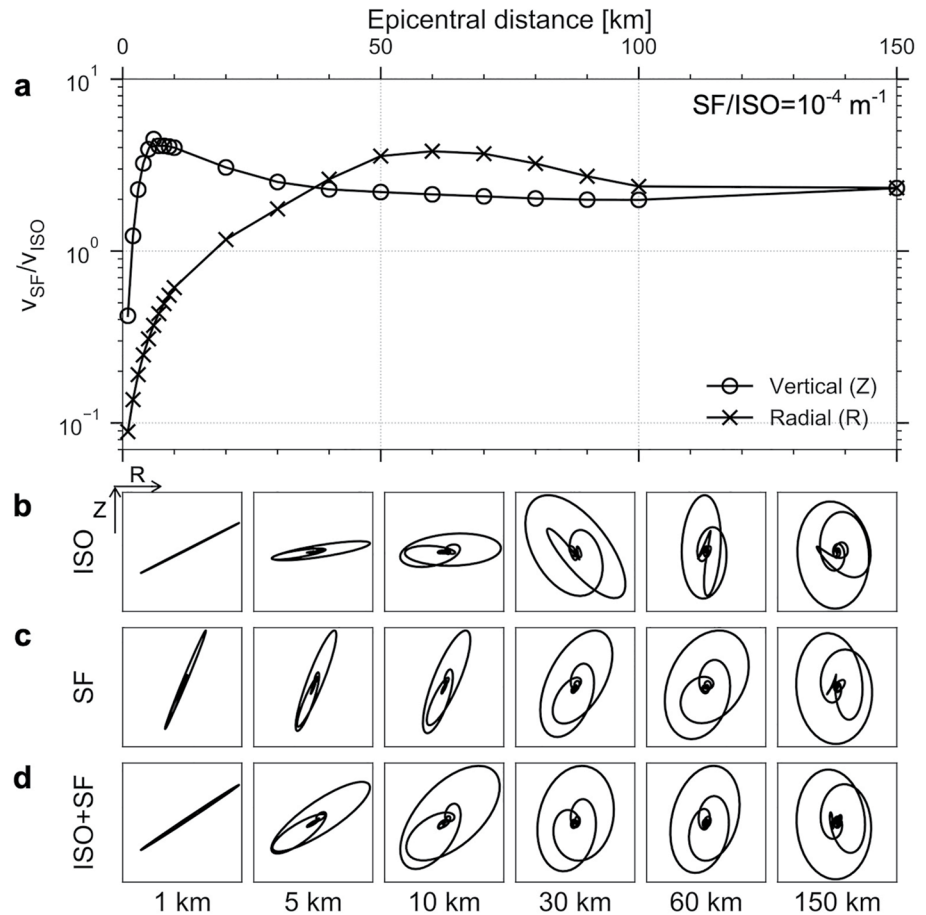
Figure 9. Contrasting waveform amplitude and particle motion between an isotropic source (ISO) and a single-force source (SF) against the epicentral distance. High very-long-period signals (VLP) band velocity amplitude ratios between the isotropic source and single-force source in the vertical (open circle) and radial (cross) components. The force is set vertical, and the force/moment ratio is fixed at 10^{-4} m^{-1}. Synthetics are calculated against a source depth of 0.5 km. (b) Example of high VLP band particle motions from an isotropic source in the vertical-radial plane. (c) Same as (a), except from a vertical single-force (SF) source. (d) Same as (a), except from an ISO + SF source with a force/moment ratio of 10^{-4} m^{-1}.

McLaughlin (1991) is not strictly valid in the near-field. To test the hypothesis further, Figure 10c displays the velocity amplitude ratios measured in the typical LP band of 1–2 Hz. As expected, the amplitude ratios are essentially constant beyond 10 km. Since the distance range of the near-field for high frequency waves is rather limited, the source equivalence of Day and McLaughlin (1991) is generally valid in the far-field (i.e., >10 km).

In short, the limitation of Day and McLaughlin (1991)'s assertion, previously pointed out by Fukao (1995), is validated by our synthetic experiment. As illustrated in Figure 10, the inclusion of distant stations in the near-field against the source modeling of single-force component shall provide a more robust constraint with a minimal tradeoff with a horizontal-crack source. Synthetic tests done by Ohminato et al. (1998) also showed that, the single-force and vertical dipole component (M_{zz}) can be resolved with near-field data and the tradeoff between single-force and horizontal crack is also relatively minimal (i.e., force/moment ratio of $\sim 10^{-6}$ m^{-1}). Since the near-field term of the single-force component decays at a slower rate than that generated from the moment tensor component (i.e., $1/r^3$ versus $1/r^4$, Aki & Richards, 2002), it is not unexpected that near-field data can help distinguish a single-force source from a horizontal-crack source (i.e., moment tensor components).

5.2.3. Single-Force Component in the VLP Source Beneath Aso Volcano?

Here we systematically explore if the addition of single-force component may reconcile the discrepancies in the high VLP band particle motions shown in Figures 8b and 8c, we examine the sensitivity of high VLP band particle motions at ASHV (i.e., $\sim$3.5 km from the SC) and TMC (i.e., $\sim$34.5 km from the SC) against the force
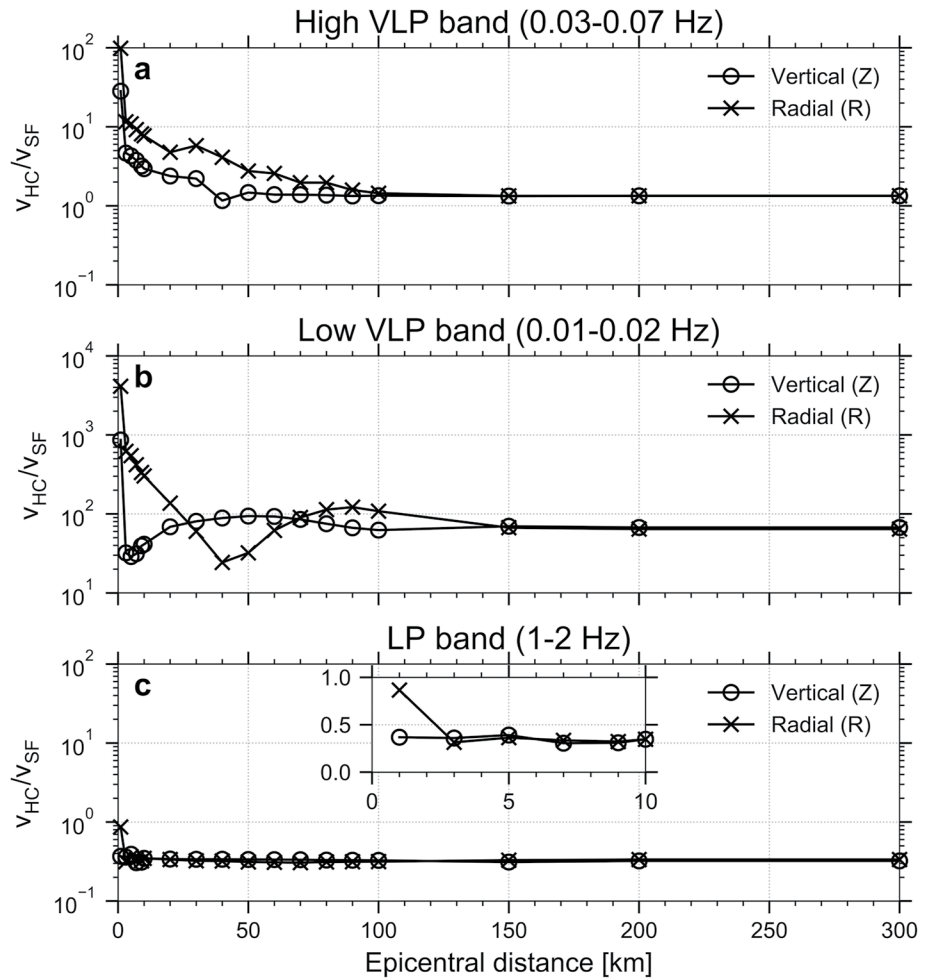
Figure 10. Contrasting velocity amplitude from a vertical single-force source and an equivalent horizontal tensile crack source against epicentral distance. (a) Peak-to-peak velocity amplitude ratio between the horizontal tensile crack (V_{HC}) and the vertical single force (V_{SF}) against epicentral distance in the high very-long-period signals (VLP) band (0.03–0.07 Hz). Open circles and crosses mark the amplitude ratio measured in the vertical and radial components, respectively. (b) and (c) Same as (a), except in the low VLP band (0.01–0.02 Hz) and long-period (LP) band (1–2 Hz), respectively. The inset in (c) zooms in the graph in the distance range of 0–10 km. The magnitude of vertical single force is 1×10^{17} N· h/v_p^2 and the moment of the equivalent horizontal tensile crack is 1×10^{17} N·m, where v_p is P wave velocity and h is source depth.

dip angle θ and force/moment ratio, assuming a constant force strike of 90°. As shown in Figure 11, the particle motions from isotropic or single-force component are generally quite different and each component alone does not explain the data, regardless the force direction. However, we find that an upward, subvertical force (i.e., ~85° from horizontal) and a force/moment ratio of ~10^{-4} m^{-1} appear to reconcile the observations quite satisfactory.

Motivated by this finding, we conduct a grid-search scheme to explore the optimal source parameters for a joint source (SF + ISO), including the force/moment ratio between the single-force component and isotropic component and the force direction, that best explain the high VLP band data of Event 1 and Event 2 at the in situ and distant stations. Except one station (STM), all stations are well within the range of near-field in the high VLP band. Following the approach by Maeda et al. (2011), we have also included the contributions from translation and tilt in the horizontal synthetic seismograms. Similar to the approach by Legrand et al. (2000), we use the filtered waveform at ASHV as the source-time function and only the amplitude at each component is used to invert for the source parameters. The misfit Δ between the data and the synthetics is defined by $\Delta = \frac{\sum_{i=1}^{N} \sum_{k=1}^{3} \|w_k(s_i^k - d_i^k)\|}{\sum_{i=1}^{N} \sum_{k=1}^{3} \|w_k d_j^k\|}$, where d_i^k is the filtered observed velocity waveforms in the kth component of the ith station; s_i^k is the filtered synthetic
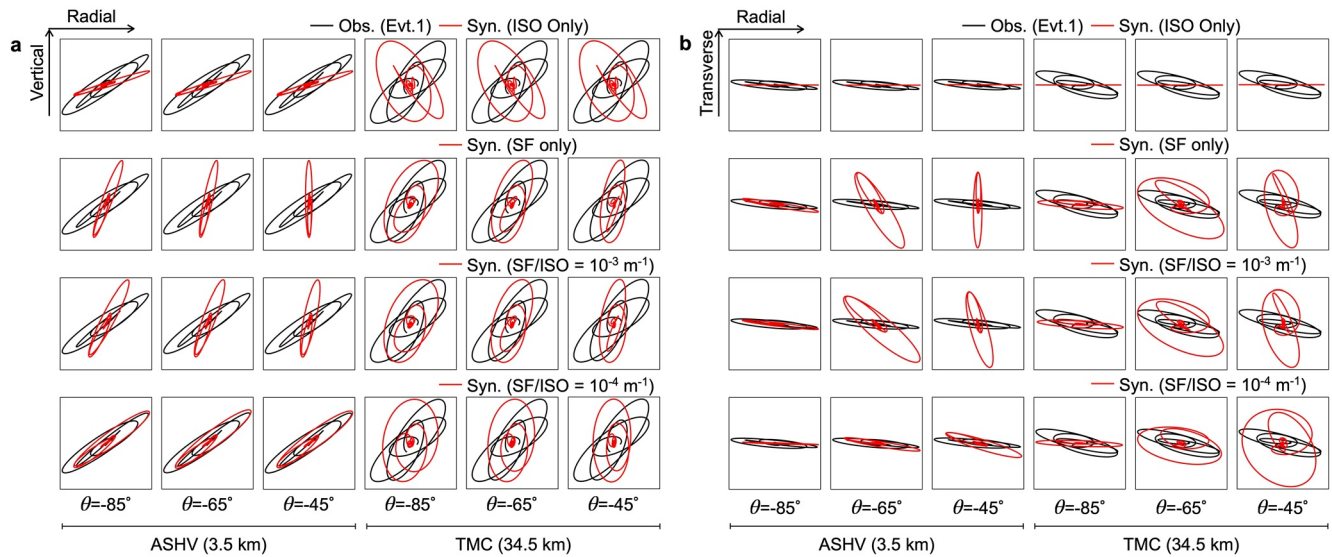
Figure 11. Forward modeling high very-long-period signals (VLP) band particle motions against isotropic and single-force sources. (a) Comparing high VLP band particle motions of Event 1 (black) against synthetics (red) in the vertical-radial plane. Top to bottom panels: synthetics are calculated from an isotropic source (ISO), a single-force (SF) source, an ISO + SF source with a force/moment ratio of 10^{-3} m^{-1}, and an ISO + SF source with a force/moment ratio of 10^{-4} m^{-1}, respectively. The SF strike is set at 90° and the dip angle θ varies from $-85°$ to $-45°$. Note the negative dip angle indicates an upward force. (b) Same as (a) except in the radial-transverse plane.

velocity waveforms in the kth component of the ith station, N is the station number and $\|*\|$ indicates two-norm; w_k is the weighting factor of the velocity waveforms in the kth component.

We note that the amplitudes of the observed waveforms in the transverse components are nearly 1/3 of the amplitudes in the radial and vertical component across all the stations. To balance the misfit calculation across all three components, we assign $w_k = 1$ for the radial and vertical components and $w_k = 3$ for the transverse component, respectively. As the number of source parameters in Legrand et al. (2000) (6 parameters) and our SF + ISO model (4 parameters) is different, we compute their *AICs* (Akaike Information Criterion, Akaike, 1974) to facilitate model selection. The *AIC* can be defined as $N_c \times N_s \times \ln(\Delta) + 2 \times m$ (i.e., Ohminato et al., 1998), where m is the number of the independent free parameters, N_c is the number of channels and N_s is the number of samples in each trace.

The preferred SF + ISO source for Event 1 (Event 2) includes an isotropic component (i.e., volume increase) of 4.18×10^{14} (4.65×10^{14}) N · m and a single-force component of 6.62×10^{10} (7.37×10^{10}) N (see also Table 2). The moment of the isotropic component in the preferred SF + ISO source is similar to that estimated from Legrand et al. (2000)'s moment tensor solution. As shown in Figure 12a (see also Figure S4a in Supporting Information S1), the SF + ISO source prefers a single-force orienting approximately toward the East and $\sim75°$ from horizontal and the preferred force/moment ratio is $\sim10^{-4}$ m^{-1} (Figure 12b, see also Figure S4b in Supporting

Table 2
Preferred Force and Moment Parameters for Event 1 and Event 2 From the Grid-Search Scheme

	Scheme	Force/Moment (m^{-1})	Strike angle (°)	Dip angle	Force (N)	Moment (N m)	$\triangle$	AIC
Event 1	ISO + SF	1.58E−04	79	−72	6.62E+10	4.18E+14	0.239	−34,402
	L2000	–	–	–	–	3.87E+14	1.500	9,756
Event 2	ISO + SF	1.58E−04	73	−72	7.37E+10	4.65E+14	0.230	−35,298
	L2000	–	–	–	–	4.31E+14	1.535	10,302

Note. The absolute magnitude of single-force and moment of ISO is scaled from the estimated force/moment ratio by fitting the amplitude of the filtered vertical velocity at N.ASHV. The moments and AICs of L2000 are calculated against the previous moment tensor solution by Legrand et al. (2000).
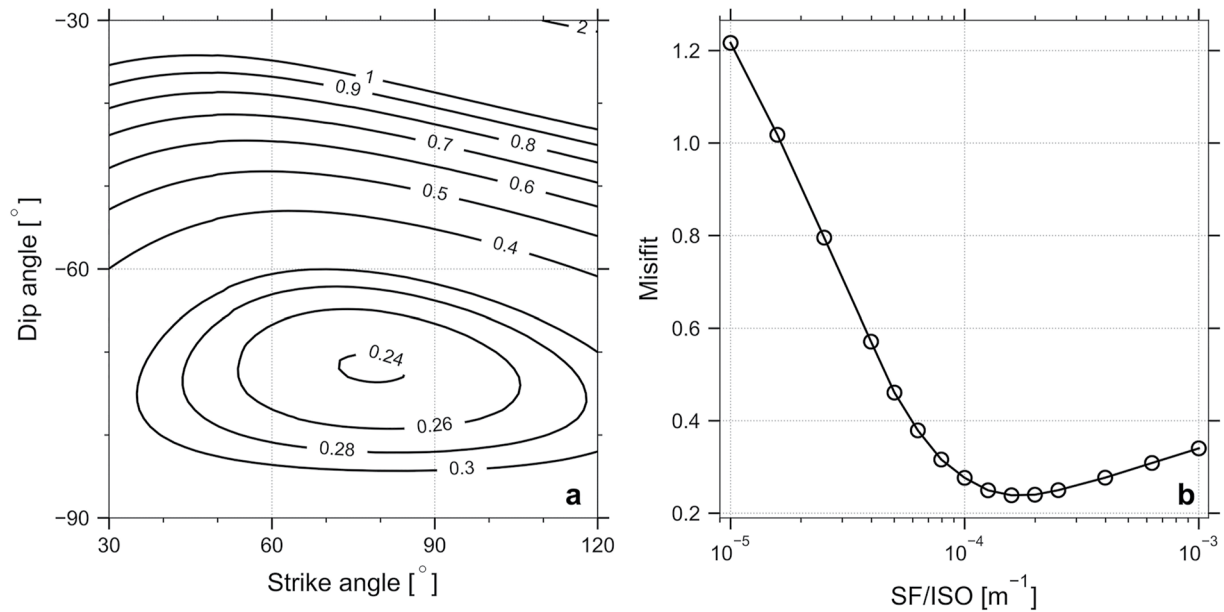
Figure 12. Grid-search result for an isotropic source + single-force source (ISO + SF) source against the single-force orientation and the force/moment ratio. (a) Misfit contours against the strike and dip angle of the single force at the preferred force/moment ratio. (b) Misfit against the force/moment ratio at the preferred force orientation.

Information S1). Such a SF + ISO source explains the data more satisfactory with a much lower misfit than the moment tensor solution of Legrand et al. (2000) (Figures 13 and 14; Figures S5 and S6 in Supporting Information S1). The AIC for such a SF + ISO source (∼−34,000) is also much lower than that for the moment tensor solution of Legrand et al. (2000) (∼10,000) (Table 2). In short, this result indicates that the two large VLPs before the 2016 phreatomagmatic eruptions likely involve a subvertical single-force component with a force/moment ratio of ∼10^{-4} m^{-1}. The force dip is apparently subparallel to the crack-like conduit previously established by Yamamoto et al. (1999), whereas the force strike is approximately normal to the strike of the crack-like conduit (Figure 15).

If we consider the crack width of 1,000 m and crack aperture of 25 m (Yamamoto, 2005; Yamamoto et al., 1999), or a cross section area A of about 25,000 m^2, the single-force magnitude F of ∼6.62×10^{10} N (∼7.37×10^{10} N) for Event 1 (Event 2) corresponds to an excess overpressure ΔP of ∼2.6 MPa (∼2.9 MPa) in the crack-like conduit
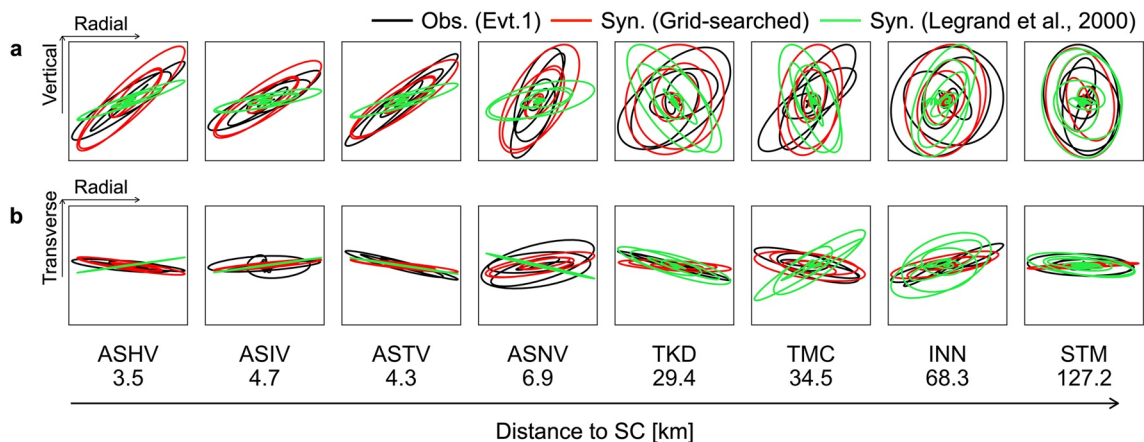
Figure 13. Observed and synthetic particle motions with the preferred single-force source + isotropic source (SF + ISO) source. (a) Comparisons of observed high VLP band particle motions of Event 1 (black) against synthetics from the preferred ISO + SF source (red) in the vertical-radial plane. Synthetics from the previous moment tensor source (Legrand et al., 2000) are shown in green. (b) Same as (a), except in the radial-transverse plane.
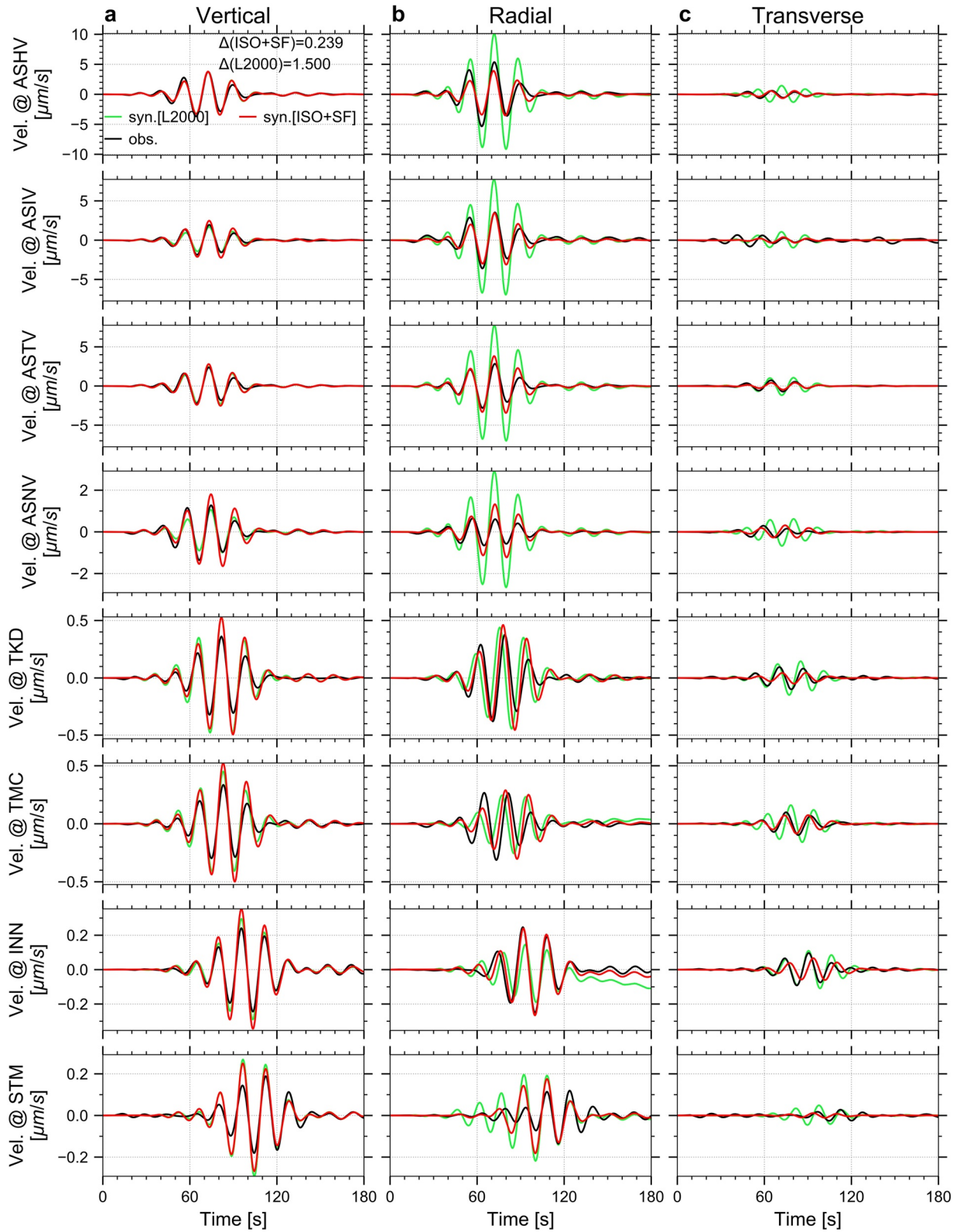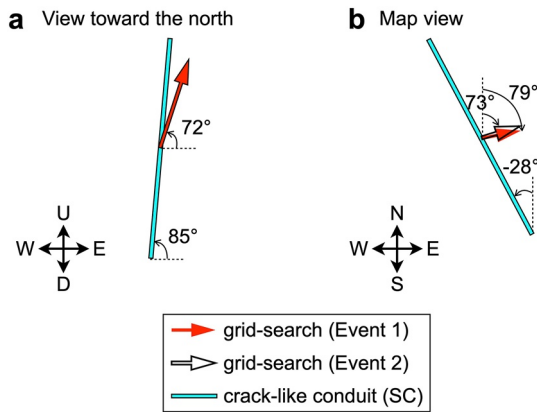
Figure 14.

Figure 15. A diagram of the single-force component against the geometry of the crack-like conduit. (a) The orientation of the preferred single-force of Event 1 (red arrow) and Event 2 (open arrow) against the crack-like conduit (SC) (blue) (Yamamoto et al., 1999) in a vertical cross section (view toward the north). (b) Same as (a), except in a map view.

before the 2016 eruption. On the other hand, the two VLPs are exceptionally large, and whether the same source property (i.e., force/moment ratio) applies to VLPs during the period of quiescence, or phreatic eruptions remains to be elaborated. While Legrand et al. (2000) explored the single-force component against VLPs during the period of phreatic eruption in 1994, the data were mostly limited at stations very close to the source (i.e., 1–2 km). There were a few stations slightly further away, but the data appear too noisy to help conclude the significance of the single-force component.

The mixed source mechanism associated with the two large pressurization VLPs (i.e., Event 1 and Event 2) includes a transient, volume increase component and an upward, subvertical force component. As a result of the exchange of momentum between the source volume and the Earth (Kawakatsu, 1989; Takei & Kumazawa, 1994, 1995), we suggest that the upward, subvertical force component is consistent with the reaction force against the deceleration of upward fluid transport. On the other hand, as noted earlier, depressurization VLP possesses very similar waveforms and particle motions to pressurization VLP, but with an opposite polarity. In this instance, depressurization VLP shall include a transient, volume decrease component and a downward, subvertical force component. The downward, subvertical force component is consistent with the reaction force against the acceleration of upward fluid transport. These inferences are generally compatible with the dominance of pressurization VLP and synchronous inflation event during volcanic unrest and depressurizaton VLP and synchronous deflation event during the Strombolian eruption, respectively.

As shown in Figure 9a, the addition of V-net (i.e., 3.5–7 km from SC) and F-net (i.e., >∼30 km from SC) provides ideal station coverage to tease out the presence of single-force component and to help elucidate if the single-force component may vary against VLPs in the 2011–2016 eruption cycle (Niu & Song, 2020). Finally, we do not rule out that strong lateral variations in velocity structures and unmodeled topography near Aso caldera may contribute to the discrepancies in the high VLP band waveforms and particle motions. While not presented in this report, our synthetic test suggests that these unmodeled effects could slightly modulate the direction of the single-force component, but the estimate of the force/moment ratio remains robust. Future work will involve 3D waveform modeling to further explore the robustness of the single-force component associated with repetitive VLPs in Aso volcano.

6. Discussions and Perspectives

In this study, we demonstrate that repetitive VLPs and synchronous deformation events beneath Aso volcano can be observed at stations even 30–1,000 km away from their sources. High-quality waveform stacks make it feasible to recognize diverse VLP and deformation events and characterize their source locations and mechanisms in high and low VLP bands, respectively. While repetitive VLP signals such as those observed in Aso may not necessarily occur in other stratovolcanoes or/and in different volcanic settings, as detailed in the following discussions, we highlight the potential of data at distant stations in source characterization and monitoring of repetitive volcanic-seismic signals in well-instrumented volcanoes such as Aso and otherwise uninstrumented volcanoes. While most efforts in the past decades have been put to address the use of in situ stations near the edifice, the use of the term "remote" in the following discussions is meant to emphasize the usage and advantage of stations that are not necessarily in close proximity to the edifice, regardless whether the stations are in the near-field and far-field.

Figure 14. Comparison of the high VLP band observations and synthetics from the preferred mixed source. (a) Comparisons of observed high VLP band vertical-component waveforms of Event 1 (black) against synthetics from the preferred isotropic source + single-force source (ISO + SF) source (red). Synthetics from the previous moment tensor source (L2000, Legrand et al., 2000) are shown in green. Synthetics are normalized against the amplitude in the vertical component at ASHV and they are aligned against the observed waveform in the vertical component at each station. (b) Same as (a), except in the radial component. (c) Same as (a), except in the transverse component. Δ (ISO + SF) and Δ (L2000) indicate the waveform misfit for the ISO + SF source and the moment tensor of (L2000, Legrand et al., 2000), respectively. The result for Event 2 can be referred to Figure S6 in Supporting Information S1.

6.1. Remote Monitoring and Source Characterization of Repetitive Volcanoseismic Signals in Aso and Other Well-Instrumented Volcanoes

As discussed Section 1, repetitive VLPs and synchronous deformation events potentially resemble different volcanic processes in different parts of the magmatic-plumbing system beneath Aso volcano (Kaneshima et al., 1996; Kawakatsu et al., 2000; Niu & Song, 2021). In particular, the prominence of pressurization VLP or depressurization VLP potentially illuminates degassing and vaporization process inside the SC as well as the strength/permeability of the conduit plug (Niu & Song, 2020). The dual signals of VLP and synchronous deformation events during the 2011–2016 unrest and eruption activities also highlight the potential of monitoring the interaction between discrete storage zones within the magma-plumbing system (Niu & Song, 2021). However, as modern in situ instrumentations such as V-net have only become publicly available since 2011, monitoring and evaluating these interactions for historical eruptions are not straightforward. Furthermore, stations close to the edifice can be at high risk during more explosive eruptions (e.g., the 2015 phreatomagmatic eruption) and data availability is not warranted. This echoes the importance of monitoring weak, repetitive volcanoseismic signals using distant stations.

While Sandanbata et al. (2015) and Hendriyana and Tsuji (2019) utilized high VLP band Rayleigh waves at the F-net stations to catalog VLP activities, it is straightforward to cluster the detected signals and distinguish pressurization VLPs from depressurization VLPs. On the other hand, it is feasible to detect the deformation events and characterize their source location/mechanism using low VLP band Rayleigh waves recorded at distant stations. Since the source of repetitive VLPs can be identified using Rayleigh waves from short-period ambient-noise cross-correlation (Zeng & Ni, 2010), we expect that the source of repetitive deformation events is detectable through long-period ambient-noise cross-correlation analysis as well. Evidently, if the event is small, source detection can be limited at distant stations.

As suggested by Niu and Song (2021), the deformation events likely represent short-lived, episodic transport of discrete magma batches between the roof of the magma chamber (Ohkura et al., 2009; Sudo et al., 2006; Sudo & Kong, 2001) and a preeruptive storage pool of mixed magma (Kawaguchi et al., 2020; Saito et al., 2018), the source validation using distant stations, as demonstrated in this report, further support such a scenario during the 2011–2016 eruption cycle. While similar processes occur in the past eruption cycles remain to be investigated, it is paramount to expand the detection of deformation events against past volcanic activities during which dedicated in situ stations near the edifice were unavailable. As noted in Section 5, the amplitude of the deformation events in Aso is generally small and it is not trivial to detect the signal without a signal enhancement procedure such as waveform stacking. However, if the deformation events are synchronous with VLPs as noted in 2011–2016, one can first construct a VLP catalog with distant stations and the timing of each VLP event can be used to stack low VLP band Rayleigh waves and retrieve the deformation events.

On the other hand, the estimated force/moment ratio for VLPs in Aso volcano (i.e., 10^{-4} m^{-1}) potentially reflects a robust process or/and scale modulating the overpressure and magma/gas transport in the shallow conduit. It will be informative to systematically reevaluate such estimates in VLPs or/and volcanoseismic signals in diverse volcanic settings and magma compositions (e.g., Chouet et al., 2003, 2005, 2010; Dawson et al., 2011; De Barros et al., 2011; Duputel & Rivera, 2019; Kim et al., 2014; Lanza & Waite, 2018; Lyons & Waite, 2011; Matoza et al., 2022; Nakano et al., 2003; Ohminato, 2006; Ohminato et al., 2006, 1998; Richardson & Waite, 2013; Uhira & Takeo, 1994; Waite et al., 2008). Cautions shall be exercised against the robustness of these estimates, especially when the estimated force/moment ratio is low. Presumably, uncertainties in the source location and unmodeled velocity structure can potentially result in a spurious single-force component (e.g., Bean et al., 2008; De Barros et al., 2011, 2013; Maeda et al., 2011).

While well-instrumented volcanoes such as Aso often focus on in situ observations near the edifice, the combination of data at in situ and distant stations should greatly improve the power in resolving the presence of single-force component in the source. Concerning the tradeoff between a single-force component and a horizontal-crack component in shallow volcanic sources, source modeling shall include data in the near-field. Furthermore, the effect of tilt on the horizontal components at distant stations, even at the high VLP or low VLP band (e.g., Maeda et al., 2011; van Driel et al., 2015), is also greatly reduced. On the other hand, it is potentially more challenging to constrain single-force source against high frequency signals such as LPs using data at distant stations.

The availability of distant stations ensures continuous monitoring of VLP and synchronous deformation events even when in situ stations near the edifice became unavailable. Except several minor eruptions in 2003–2005 (Miyabuchi et al., 2008), Aso volcano was mostly quiescent between 1991 and 2010. Expanding the detection of VLP and deformation events from 1991 to 2010 using the F-net stations could substantially improve our understandings of the feedback between the SC and SMSZ in the past three decades. Nevertheless, the example in Aso highlights the potential of remote detection and verification of repetitive volcanoseismic signals in other well-instrumented volcanoes in Japan (e.g., Maeda & Takeo, 2011; Yamamoto et al., 2002) and around the world (e.g., Chouet & Matoza, 2013; Park et al., 2020; Waite et al., 2008).

6.2. Remote Monitoring Against Uninstrumented Volcanoes

Only 10% of inland active volcanoes are monitored systematically (e.g., Poland, 2015). Space and aerial borne sensors, such as Interferometric Synthetic Aperture Radar (InSAR) (e.g., Biggs et al., 2011, 2014; Chaussard et al., 2013; Dzurisin, 2006; Ebmeier et al., 2018; Fournier et al., 2010; Lu & Dzurisin, 2014; Pinel et al., 2014; Pritchard & Simons, 2002; Reath et al., 2019) help identify surface deformation in uninstrumented volcanoes globally. The detection and characterization of repetitive volcanoseismic signals critical to the transport of magma and hydrothermal fluids within the magma plumbing system remain limited in well-instrumented volcanoes (e.g., Chouet & Matoza, 2013). As illustrated in this report, it is potentially feasible to detect and characterize repetitive volcanoseismic signals remotely in uninstrumented volcanoes using continuous waveform recordings from established seismic networks. In particular, recent ambient-noise cross-correlation analyses have demonstrated the capability of detecting repetitive tremor-like signals from a persistent and localized source (e.g., Shapiro et al., 2006; Xia & Chen, 2020; Xia et al., 2013; Zeng & Ni, 2010, 2014), offering a new venue to systematically detect repetitive volcanoseismic signal using observations at distant stations.

Figure 16 summarizes the capacity of remote monitoring against ~1,400 volcanoes with eruptions during the Holocene period (<10,000 years). Here we consider global broadband high-gain BH and HH channels from the Incorporated Research Institutions of Seismology (IRIS) and the permanent F-net and V-net seismic stations from NIED. As an example, Figure 16a shows that 5–15% (10–30%) of global Holocene volcanoes are surrounded by at least four broadband seismic stations within 50 km (100 km). In general, the fraction of volcanoes surrounded by more than four stations increases by a factor of 2–3 over the past ~20 years. In Japan, the permanent broadband seismic network F-net has been established since 1999. While 20%–35% of Japanese volcanoes are surrounded by more than four F-net stations within 100 km (Figure 16b), the establishment of V-net since 2011 greatly improves the station coverage within 50 km, resulting in the coverage up to 30% of active volcanoes in Japan (Figure 16c). Interestingly, among Holocene volcanoes previously surveyed by remote sensing (e.g., InSAR, Biggs & Pritchard, 2017), 10%–25% (15%–50%) of these volcanoes are surrounded by at least four broadband stations within 50 km (100 km) (Figure 16d) and they are mostly located in Alaska-Aleutian, South America, Central America, Hawaii, Kyushu, North Izu-Bonin, central Mariana and the Northwest United States (Figure 16e; Figures S7, S8, and Table S1 in Supporting Information S1). Opportunities also exist in the Caribbean and Africa, especially in 2005–2015 (Figures S7, S8, and Table S1 in Supporting Information S1).

Presumably, joint analysis of remote seismic and geodetic monitoring provides a new gateway to a more comprehensive understanding of magmatic/nonmagmatic processes and the nature of surface deformation in uninstrumented volcanoes. While numerous volcanoes are surrounded by only 1–2 stations within 50 km (Figure 16e and Figure S8 in Supporting Information S1), even one broadband seismic station can potentially provide a critical monitoring opportunity (e.g., Fontaine et al., 2019; Lemoine et al., 2020). Facilitated by machine learning (e.g., Falcin et al., 2021; Langer et al., 2009; Maeda et al., 2021; Malfante et al., 2018; Manley et al., 2020; Titos et al., 2018), seismic monitoring efforts may be performed in concert with satellite remote sensing, including surface deformation, SO_2 degassing and thermal output (e.g., Newhall et al., 2017; Reath et al., 2019), to interrogate the magma/gas transport within the transcrustal magmatic system during the quiescence and volcanic unrest in the preeruptive period. Such efforts focusing on the preeruptive periods complement infrasound monitoring during the syneruptive episodes (e.g., Matoza et al., 2019; McKee et al., 2021) and potentially help facilitate precursory analysis of upcoming eruptions and hazard mitigation (e.g., Dempsey et al., 2020).

Lastly, seismic monitoring of submarine volcanoes (e.g., D'Alessandro et al., 2009; Dziak et al., 2008, 2012; Fukao et al., 2018; Konter et al., 2004; Kudo et al., 1991; Lindsay et al., 2005; Wright et al., 2008; Watts et al., 2012; Wilcock et al., 2016; Yamasato et al., 1991) or axial volcanoes in mid-ocean ridges (e.g., Schlindwein
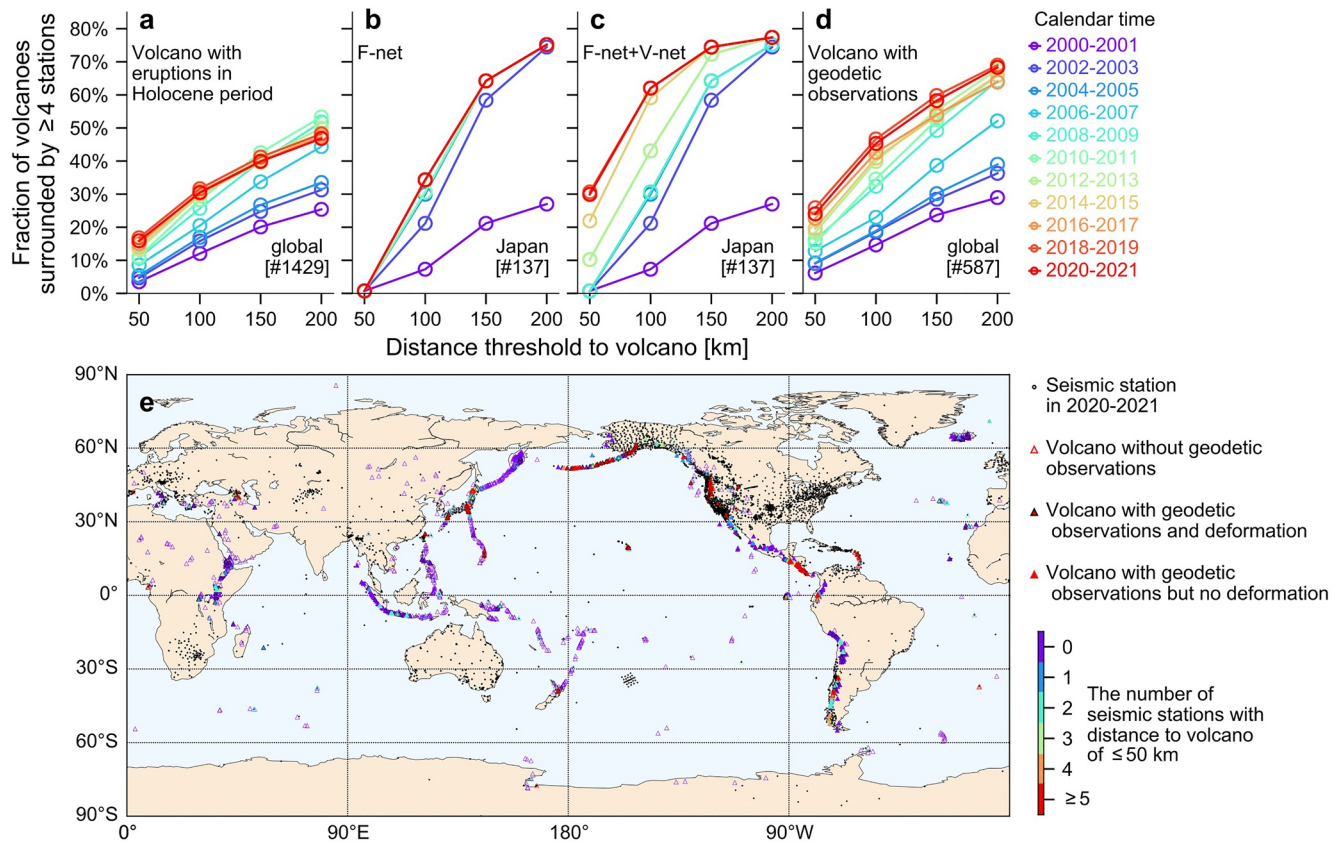
Figure 16. Global remote detection and monitoring of repetitive volcanoseismic signals. (a) The fraction of global Holocene volcanoes (<10,000 years) surrounded by ≥4 global broadband seismic stations (Incorporated Research Institutions of Seismology (IRIS), BH, and HH channels) in selected distance threshold in different observation periods. The locations of 1,398 global volcanoes are provided by the Global Volcanism Program (Smithsonian Institution & Venzke, 2013). The number in the bottom-right corner shows the total number of volcanoes in the analysis. (b) The fraction of active volcanoes in Japan surrounded by ≥4 F-net broadband seismic stations in selected distance threshold in different observation periods. The locations of 110 active volcanoes with 137 active cones in Japan are provided by JMA (https://www.data.jma.go.jp/svd/vois/data/tokyo/STOCK/souran_eng/menu.htm). (c) Same as (b), except displaying the result against F-net and V-net seismic stations. (d) Same as (a), except considering Holocene volcanoes surveyed by geodetic observations. (e) A map view of global detection and monitoring capacity in 2020–2021. The geographical locations of global broadband seismic stations are shown as black circles. Volcanoes with no geodetic observations, volcanoes with geodetic observations and reported deformation, and volcanoes with geodetic observations but no deformation are shown as open triangles, enclosed filled triangles, and filled triangles, respectively, color-coded by the number of broadband stations within 50 km.

et al., 2005; Schmid et al., 2017; Tolstoy et al., 2001, 2006) can benefit from the deployment of ocean bottom sensors (e.g., seismometers, hydrophones), although observations have predominantly focused on volcanotectonic earthquakes (VTs) and tremors. While a systematic detection and monitoring of repetitive volcanoseismic signals such as VLP or LP remain to be explored, future seismic monitoring may be coupled with hydroacoustics monitoring (e.g., Lyons et al., 2019; Tepp et al., 2020; Wech et al., 2018), sea-floor geodesy (e.g., Bürgmann & Chadwell, 2014; Chadwick et al., 2012; De Martino et al., 2020; Nooner & Chadwick, 2009) and global analysis of nondouble-couple events (e.g., Sandanbata et al., 2021; Shuler et al., 2013) to untangle the magma storage and ascent beneath submarine and axial volcanoes that remain largely unexplored.

Data Availability Statement

The seismic datasets from NIED V-net (https://doi.org/10.17598/nied.0006) and F-net (https://doi.org/10.17598/nied.0005) can be downloaded from https://www.hinet.bosai.go.jp. The waveforms data sets can be obtained through the Continuous waveform data portal after user registration. The user can choose specific network (i.e., F-net, V-net) and download continuous data in 1-min segments. The downloaded data are in the WIN format, and they can be converted to SAC format through the utility package WIN2SAC provided by Hinet. Data

processing and production of figures are implemented in Python with relevant modules such as ObsPy (https://doi.org/10.5281/zenodo.3674646) and Matplotlib (https://doi.org/10.5281/zenodo.592536).

References

Akaike, H. (1974). A new look at the statistical model identification. *IEEE Transactions on Automatic Control*, *19*(6), 716–723. https://doi.org/10.1109/TAC.1974.1100705

Aki, K., & Richards, P. G. (2002). *Quantitative seismology* (2nd ed.). University Science Book.

Bean, C., Lokmer, I., & O'Brien, G. (2008). Influence of near-surface volcanic structure on long-period seismic signals and on moment tensor inversions: Simulated examples from Mount Etna. *Journal of Geophysical Research*, *113*, B08308. https://doi.org/10.1029/2007JB005468

Bell, A., Kilburn, C., & Main, I. (2016). Volcanic eruptions, real-time forecasting of. *Encyclopedia of earthquake engineering* (pp. 3892–3906). Springer. https://doi.org/10.1007/978-3-642-36197-5_43-1

Bell, A. F., Naylor, M., Hernandez, S., Main, I. G., Gaunt, H. E., Mothes, P., & Ruiz, M. (2018). Volcanic eruption forecasts from accelerating rates of drumbeat long-period earthquakes. *Geophysical Research Letters*, *45*, 1339–1348. https://doi.org/10.1002/2017GL076429

Biggs, J., Bastow, I., Keir, D., & Lewi, E. (2011). Pulses of deformation reveal frequently recurring shallow magmatic activity beneath the Main Ethiopian Rift. *Geochemistry, Geophysics, Geosystems*, *12*, Q0AB10. https://doi.org/10.1029/2011GC003662

Biggs, J., Ebmeier, S., Aspinall, W., Lu, Z., Pritchard, M., Sparks, R., & Mather, T. (2014). Global link between deformation and volcanic eruption quantified by satellite imagery. *Nature Communications*, *5*(1), 1–7. https://doi.org/10.1038/ncomms4471

Biggs, J., & Pritchard, M. E. (2017). Global volcano monitoring: What does it mean when volcanoes deform? *Elements*, *13*(1), 17–22. https://doi.org/10.2113/gselements.13.1.17

Burger, R. W., & Langston, C. A. (1985). Source mechanism of the May 18, 1980, Mount St. Helens eruption from regional surface waves. *Journal of Geophysical Research*, *90*(B9), 7653–7664. https://doi.org/10.1029/JB090iB09p07653

Bürgmann, R., & Chadwell, D. (2014). Seafloor geodesy. *Annual Review of Earth and Planetary Sciences*, *42*, 509–534. https://doi.org/10.1146/annurev-earth-060313-054953

Cashman, K. V., Sparks, R. S. J., & Blundy, J. D. (2017). Vertically extensive and unstable magmatic systems: A unified view of igneous processes. *Science*, *355*(6331), eaag3055. https://doi.org/10.1126/science.aag3055

Cesca, S., Letort, J., Razafindrakoto, H. N., Heimann, S., Rivalta, E., Isken, M. P., et al. (2020). Drainage of a deep magma reservoir near Mayotte inferred from seismicity and deformation. *Nature Geoscience*, *13*(1), 87–93. https://doi.org/10.1038/s41561-019-0505-5

Chadwick, W. W., Nooner, S. L., Butterfield, D. A., & Lilley, M. D. (2012). Seafloor deformation and forecasts of the April 2011 eruption at Axial Seamount. *Nature Geoscience*, *5*(7), 474–477. https://doi.org/10.1038/ngeo1464

Chaussard, E., Amelung, F., & Aoki, Y. (2013). Characterization of open and closed volcanic systems in Indonesia and Mexico using InSAR time series. *Journal of Geophysical Research: Solid Earth*, *118*, 3957–3969. https://doi.org/10.1002/jgrb.50288

Chouet, B., Dawson, P., & Arciniega-Ceballos, A. (2005). Source mechanism of Vulcanian degassing at Popocatépetl Volcano, Mexico, determined from waveform inversions of very long period signals. *Journal of Geophysical Research*, *110*, B07301. https://doi.org/10.1029/2004JB003524

Chouet, B., Dawson, P., Ohminato, T., Martini, M., Saccorotti, G., Giudicepietro, F., et al. (2003). Source mechanisms of explosions at Stromboli volcano, Italy, determined from moment-tensor inversions of very-long-period data: Source mechanisms of explosion at Stromboli source. *Journal of Geophysical Research*, *108*(B1), 2019. https://doi.org/10.1029/2002JB001919

Chouet, B. A. (1996). Long-period volcano seismicity: Its source and use in eruption forecasting. *Nature*, *380*(6572), 309–316. https://doi.org/10.1038/380309a0

Chouet, B. A., Dawson, P. B., James, M. R., & Lane, S. J. (2010). Seismic source mechanism of degassing bursts at Kilauea Volcano, Hawaii: Results from waveform inversion in the 10–50 s band. *Journal of Geophysical Research*, *115*, B09311. https://doi.org/10.1029/2009JB006661

Chouet, B. A., & Matoza, R. S. (2013). A multi-decadal view of seismic methods for detecting precursors of magma movement and eruption. *Journal of Volcanology and Geothermal Research*, *252*, 108–175. https://doi.org/10.1016/j.jvolgeores.2012.11.013

Chouet, B. A., Page, R. A., Stephens, C. D., Lahr, J. C., & Power, J. A. (1994). Precursory swarms of long-period events at Redoubt Volcano (1989–1990), Alaska: Their origin and use as a forecasting tool. *Journal of Volcanology and Geothermal Research*, *62*(1–4), 95–135. https://doi.org/10.1016/0377-0273(94)90030-2

Crozier, J., & Karlstrom, L. (2021). Wavelet-Based characterization of very-long-period seismicity reveals temporal evolution of shallow magma system over the 2008–2018 eruption of Kīlauea volcano. *Journal of Geophysical Research: Solid Earth*, *126*, e2020JB020837. https://doi.org/10.1029/2020JB020837

Cruz, F. G., & Chouet, B. A. (1997). Long-period events, the most characteristic seismicity accompanying the emplacement and extrusion of a lava dome in Galeras Volcano, Colombia, in 1991. *Journal of Volcanology and Geothermal Research*, *77*(1–4), 121–158. https://doi.org/10.1016/S0377-0273(96)00091-1

Cruz-Atienza, V., Pacheco, J., Singh, S., Shapiro, N., Valdés, C., & Iglesias, A. (2001). Size of Popocatépetl volcano explosions (1997–2001) from waveform inversion. *Geophysical Research Letters*, *28*, 4027–4030. https://doi.org/10.1029/2001GL013207

Cusano, P., Palo, M., & West, M. (2015). Long-period seismicity at Shishaldin volcano (Alaska) in 2003–2004: Indications of an upward migration of the source before a minor eruption. *Journal of Volcanology and Geothermal Research*, *291*, 14–24. https://doi.org/10.1016/j.jvolgeores.2014.12.008

D'Alessandro, A., D'Anna, G., Luzio, D., & Mangano, G. (2009). The INGV's new OBS/H: Analysis of the signals recorded at the Marsili submarine volcano. *Journal of Volcanology and Geothermal Research*, *183*(1–2), 17–29. https://doi.org/10.1016/j.jvolgeores.2009.02.008

Dawson, P., & Chouet, B. (2014). Characterization of very-long-period seismicity accompanying summit activity at Kīlauea volcano, Hawai'i: 2007–2013. *Journal of Volcanology and Geothermal Research*, *278–279*, 59–85. https://doi.org/10.1016/j.jvolgeores.2014.04.010

Dawson, P., & Chouet, B. (2019). Long period seismicity at Mammoth mountain, California. *Journal of Geophysical Research: Solid Earth*, *124*, 6751–6778. https://doi.org/10.1029/2019JB017580

Dawson, P. B., Chouet, B. A., & Power, J. (2011). Determining the seismic source mechanism and location for an explosive eruption with limited observational data: Augustine Volcano, Alaska: Eruption mechanism at Augustine. *Geophysical Research Letters*, *38*, L03302. https://doi.org/10.1029/2010GL045977

Day, S. M., & McLaughlin, K. L. (1991). Seismic source representations for spall. *Bulletin of the Seismological Society of America*, *81*(1), 191–201. https://doi.org/10.1785/bssa0810010191

De Barros, L., Lokmer, I., & Bean, C. J. (2013). Origin of spurious single forces in the source mechanism of volcanic seismicity. *Journal of Volcanology and Geothermal Research*, *262*, 1–6. https://doi.org/10.1016/j.jvolgeores.2013.06.006

De Barros, L., Lokmer, I., Bean, C. J., O'Brien, G. S., Saccorotti, G., Métaxian, J.-P., et al. (2011). Source mechanism of long-period events recorded by a high-density seismic network during the 2008 eruption on Mount Etna. *Journal of Geophysical Research*, *116*, B01304. https://doi.org/10.1029/2010JB007629

De Martino, P., Guardato, S., Donnarumma, G. P., Dolce, M., Trombetti, T., Chierici, F., et al. (2020). Four years of continuous seafloor displacement measurements in the Campi Flegrei caldera. *Frontiers of Earth Science*, *8*, 641. https://doi.org/10.3389/feart.2020.615178

Dempsey, D., Cronin, S. J., Mei, S., & Kempa-Liehr, A. W. (2020). Automatic precursor recognition and real-time forecasting of sudden explosive volcanic eruptions at Whakaari, New Zealand. *Nature Communications*, *11*(1), 1–8. https://doi.org/10.1038/s41467-020-17375-2

Duputel, Z., & Rivera, L. (2019). The 2007 caldera collapse of Piton de la Fournaise volcano: Source process from very-long-period seismic signals. *Earth and Planetary Science Letters*, *527*, 115786. https://doi.org/10.1016/j.epsl.2019.115786

Dziak, R., Haxel, J., Bohnenstiehl, D., Chadwick, W., Nooner, S. L., Fowler, M., et al. (2012). Seismic precursors and magma ascent before the April 2011 eruption at Axial Seamount. *Nature Geoscience*, *5*(7), 478–482. https://doi.org/10.1038/ngeo1490

Dziak, R., Haxel, J., Matsumoto, H., Lau, T., Merle, S., De Ronde, C. E. J., et al. (2008). Observations of regional seismicity and local harmonic tremor at Brothers volcano, south Kermadec arc, using an ocean bottom hydrophone array. *Journal of Geophysical Research*, *113*, B08S04. https://doi.org/10.1029/2007JB005533

Dziewonski, A. M., & Anderson, D. L. (1981). Preliminary reference Earth model. *Physics of the Earth and Planetary Interiors*, *25*(4), 297–356. https://doi.org/10.1016/0031-9201(81)90046-7

Dzurisin, D. (2006). *Volcano deformation: New geodetic monitoring techniques*. Springer Science & Business Media.

Ebmeier, S., Andrews, B., Araya, M., Arnold, D., Biggs, J., Cooper, C., et al. (2018). Synthesis of global satellite observations of magmatic and volcanic deformation: Implications for volcano monitoring & the lateral extent of magmatic domains. *Journal of Applied Volcanology*, *7*(1), 1–26. https://doi.org/10.1186/s13617-018-0071-3

Falcin, A., Métaxian, J.-P., Mars, J., Stutzmann, É., Komorowski, J.-C., Moretti, R., et al. (2021). A machine-learning approach for automatic classification of volcanic seismicity at La Soufrière Volcano, Guadeloupe. *Journal of Volcanology and Geothermal Research*, *411*, 107151. https://doi.org/10.1016/j.jvolgeores.2020.107151

Fee, D., Izbekov, P., Kim, K., Yokoo, A., Lopez, T., Prata, F., et al. (2017). Eruption mass estimation using infrasound waveform inversion and ash and gas measurements: Evaluation at Sakurajima Volcano, Japan. *Earth and Planetary Science Letters*, *480*, 42–52. https://doi.org/10.1016/j.epsl.2017.09.043

Fee, D., & Matoza, R. (2013). An overview of volcano infrasound: From Hawaiian to Plinian, local to global. *Journal of Volcanology and Geothermal Research*, *249*, 123–139. https://doi.org/10.1016/j.jvolgeores.2012.09.002

Fontaine, F. R., Roult, G., Hejrani, B., Michon, L., Ferrazzini, V., Barruol, G., et al. (2019). Very-and-ultra-long-period seismic signals prior to and during caldera formation on La Réunion Island. *Scientific Reports*, *9*(1), 1–15. https://doi.org/10.1038/s41598-019-44439-1

Fournier, T., Pritchard, M., & Riddick, S. (2010). Duration, magnitude, and frequency of subaerial volcano deformation events: New results from Latin America using InSAR and a global synthesis. *Geochemistry, Geophysics, Geosystems*, *11*, Q01003. https://doi.org/10.1029/2009GC002558

Frank, W. B., Shapiro, N. M., & Gusev, A. A. (2018). Progressive reactivation of the volcanic plumbing system beneath Tolbachik volcano (Kamchatka, Russia) revealed by long-period seismicity. *Earth and Planetary Science Letters*, *493*, 47–56. https://doi.org/10.1016/j.epsl.2018.04.018

Fukao, Y. (1995). Single-force representation of earthquakes due to landslides or the collapse of caverns. *Geophysical Journal International*, *122*(1), 243–248. https://doi.org/10.1111/j.1365-246x.1995.tb03551.x

Fukao, Y., Sandanbata, O., Sugioka, H., Ito, A., Shiobara, H., Watada, S., & Satake, K. (2018). Mechanism of the 2015 volcanic tsunami earthquake near Torishima, Japan. *Science Advances*, *4*(4), eaao0219. https://doi.org/10.1126/sciadv.aao0219

Hase, H., Hashimoto, T., Sakanaka, S., Kanda, W., & Tanaka, Y. (2005). Hydrothermal system beneath Aso volcano as inferred from self-potential mapping and resistivity structure. *Journal of Volcanology and Geothermal Research*, *143*(4), 259–277. https://doi.org/10.1016/j.jvolgeores.2004.12.005

Hashida, T. (1990). Long-period micro-tremors observed in the Kyushu district, as excited by 1989 volcanic activity of the Aso Naka-dake. *Bulletin of the Volcanological Society of Japan*, *35*, 323–326.

Hata, M., Matsushima, N., Takakura, S., Utsugi, M., Hashimoto, T., & Uyeshima, M. (2018). Three-dimensional electrical resistivity modeling to elucidate the crustal magma supply system beneath Aso caldera, Japan. *Journal of Geophysical Research: Solid Earth*, *123*, 6334–6346. https://doi.org/10.1029/2018JB015951

Hata, M., Takakura, S., Matsushima, N., Hashimoto, T., & Utsugi, M. (2016). Crustal magma pathway beneath Aso caldera inferred from three-dimensional electrical resistivity structure: Crustal magma pathway in Aso caldera. *Geophysical Research Letters*, *43*, 10720–10727. https://doi.org/10.1002/2016GL070315

Hendriyana, A., & Tsuji, T. (2019). Migration of very long period seismicity at Aso volcano, Japan, associated with the 2016 Kumamoto earthquake. *Geophysical Research Letters*, *46*, 8763–8771. https://doi.org/10.1029/2019GL082645

Huang, Y.-C., Ohkura, T., Kagiyama, T., Yoshikawa, S., & Inoue, H. (2018). Shallow volcanic reservoirs and pathways beneath Aso caldera revealed using ambient seismic noise tomography. *Earth Planets and Space*, *70*(1), 169. https://doi.org/10.1186/s40623-018-0941-2

Jolly, A. D., Lokmer, I., Thun, J., Salichon, J., Fry, B., & Chardot, L. (2017). Insights into fluid transport mechanisms at White Island from analysis of coupled very long-period (VLP), long-period (LP) and high-frequency (HF) earthquakes. *Journal of Volcanology and Geothermal Research*, *343*, 75–94. https://doi.org/10.1016/j.jvolgeores.2017.06.006

Kanamori, H., Ekström, G., Dziewonski, A., Barker, J. S., & Sipkin, S. A. (1993). Seismic radiation by magma injection: An anomalous seismic event near Tori Shima, Japan. *Journal of Geophysical Research*, *98*(B4), 6511–6522. https://doi.org/10.1029/92JB02867

Kanamori, H., & Given, J. W. (1982). Analysis of long-period seismic waves excited by the May 18, 1980, eruption of Mount St. Helens—A terrestrial monopole? *Journal of Geophysical Research*, *87*(B7), 5422–5432. https://doi.org/10.1029/JB087iB07p05422

Kanamori, H., Given, J. W., & Lay, T. (1984). Analysis of seismic body waves excited by the Mount St. Helens eruption of May 18, 1980. *Journal of Geophysical Research*, *89*(B3), 1856–1866. https://doi.org/10.1029/JB089iB03p01856

Kanamori, H., & Mori, J. (1992). Harmonic excitation of mantle Rayleigh waves by the 1991 eruption of Mount Pinatubo, Philippines. *Geophysical Research Letters*, *19*(7), 721–724. https://doi.org/10.1029/92GL00258

Kanamori, H., Mori, J., & Harkrider, D. G. (1994). Excitation of atmospheric oscillations by volcanic eruptions. *Journal of Geophysical Research*, *99*(B11), 21947–21961. https://doi.org/10.1029/94JB01475

Kanda, W., Utsugi, M., Takakura, S., & Inoue, H. (2019). Hydrothermal system of the active crater of Aso volcano (Japan) inferred from a three-dimensional resistivity structure model. *Earth Planets and Space*, *71*(1), 37. https://doi.org/10.1186/s40623-019-1017-7

Kaneshima, S., Kawakatsu, H., Matsubayashi, H., Sudo, Y., Tsutsui, T., Ohminato, T., et al. (1996). Mechanism of phreatic eruptions at Aso volcano inferred from near-field broadband seismic observations. *Science*, *273*(5275), 643–645. https://doi.org/10.1126/science.273.5275.643

Kawaguchi, M., Hasenaka, T., Koga, K., Rose-Koga, E., Yasuda, A., Hokanishi, N., et al. (2020). Persistent gas emission originating from a deep basaltic magma reservoir of an active volcano: The case of Aso volcano, Japan. *Contributions to Mineralogy and Petrology*, *176*, 6. https://doi.org/10.1007/s00410-020-01761-6

Kawakatsu, H. (1989). Centroid single force inversion of seismic waves generated by landslides. *Journal of Geophysical Research*, *94*(B9), 12363–12374. https://doi.org/10.1029/JB094iB09p12363

Kawakatsu, H., Kaneshima, S., Matsubayashi, H., Ohminato, T., Sudo, Y., Tsutsui, T., et al. (2000). Aso94: Aso seismic observation with broadband instruments. *Journal of Volcanology and Geothermal Research*, *101*(1–2), 129–154. https://doi.org/10.1016/S0377-0273(00)00166-9

Kawakatsu, H., Ohminato, T., & Ito, H. (1994). 10s-period volcanic tremors observed over a wide area in southwestern Japan. *Geophysical Research Letters*, *21*(18), 1963–1966. https://doi.org/10.1029/94GL01683

Kawakatsu, H., & Yamamoto, M. (2007). Volcano seismology. In *Treatise on geophysics* (1st ed., Vol. 4, pp. 389–420). Elsevier. https://doi.org/10.1016/b978-044452748-6.00073-0

Kawano, Y., Isse, T., Takeo, A., Kawakatsu, H., Suetsugu, D., Shiobara, H., et al. (2020). Persistent long-period signals recorded by an OBS array in the western-central Pacific: Activity of ambrym volcano in Vanuatu. *Geophysical Research Letters*, *47*, e2020GL089108. https://doi.org/10.1029/2020GL089108

Kennett, B. L. N., Engdahl, E. R., & Buland, R. (1995). Constraints on seismic velocities in the Earth from traveltimes. *Geophysical Journal International*, *122*(1), 108–124. https://doi.org/10.1111/j.1365-246X.1995.tb03540.x

Kim, K., Lees, J. M., & Ruiz, M. C. (2014). Source mechanism of Vulcanian eruption at Tungurahua Volcano, Ecuador, derived from seismic moment tensor inversions. *Journal of Geophysical Research: Solid Earth*, *119*, 1145–1164. https://doi.org/10.1002/2013JB010590

Konter, J. G., Staudigel, H., Hart, S. R., & Shearer, P. (2004). Seafloor seismic monitoring of an active submarine volcano: Local seismicity at Vailulu'u Seamount, Samoa. *Geochemistry, Geophysics, Geosystems*, *5*, Q06007. https://doi.org/10.1029/2004GC000702

Kubotera, A. (1974). Volcanic tremors at Aso volcano. In *Developments in Solid Earth Geophysics* (Vol. 6, pp. 29–47). Elsevier. https://doi.org/10.1016/b978-0-444-41141-9.50008-5

Kudo, K., Sawada, M., Sakaue, M., Miyazaki, T., & Oshima, S. (1991). Volcanic tremor associated with the 1989 submarine eruption off Ito, Japan. *Journal of Physics of the Earth*, *39*(1), 27–45. https://doi.org/10.4294/jpe1952.39.27

Langer, H., Falsaperla, S., Masotti, M., Campanini, R., Spampinato, S., & Messina, A. (2009). Synopsis of supervised and unsupervised pattern classification techniques applied to volcanic tremor data at Mt Etna, Italy. *Geophysical Journal International*, *178*(2), 1132–1144. https://doi.org/10.1111/j.1365-246X.2009.04179.x

Lanza, F., & Waite, G. P. (2018). Nonlinear moment-tensor inversion of repetitive long-periods events recorded at Pacaya volcano, Guatemala. *Frontiers of Earth Science*, *6*, 139. https://doi.org/10.3389/feart.2018.00139

Legrand, D., Kaneshima, S., & Kawakatsu, H. (2000). Moment tensor analysis of near-field broadband waveforms observed at Aso volcano, Japan. *Journal of Volcanology and Geothermal Research*, *101*(1–2), 155–169. https://doi.org/10.1016/S0377-0273(00)00167-0

Lemoine, A., Briole, P., Bertil, D., Roullé, A., Foumelis, M., Thinon, I., et al. (2020). The 2018–2019 seismo-volcanic crisis east of Mayotte, Comoros islands: Seismicity and ground deformation markers of an exceptional submarine eruption. *Geophysical Journal International*, *223*(1), 22–44. https://doi.org/10.1093/gji/ggaa273

Lindsay, J. M., Shepherd, J. B., & Wilson, D. (2005). Volcanic and scientific activity at Kick'em Jenny submarine volcano 2001–2002: Implications for volcanic hazard in the southern Grenadines, lesser Antilles. *Natural Hazards*, *34*(1), 1–24. https://doi.org/10.1007/s11069-004-1566-2

Lokmer, I., Saccorotti, G., Di Lieto, B., & Bean, C. J. (2008). Temporal evolution of long-period seismicity at Etna Volcano, Italy, and its relationships with the 2004–2005 eruption. *Earth and Planetary Science Letters*, *266*(1–2), 205–220. https://doi.org/10.1016/j.epsl.2007.11.017

Lu, Z., & Dzurisin, D. (2014). InSAR imaging of Aleutian volcanoes. In *InSAR imaging of Aleutian volcanoes* (pp. 87–345). Springer. https://doi.org/10.1007/978-3-642-00348-6_6

Lyons, J. J., Haney, M. M., Fee, D., Wech, A. G., & Waythomas, C. F. (2019). Infrasound from giant bubbles during explosive submarine eruptions. *Nature Geoscience*, *12*(11), 952–958. https://doi.org/10.1038/s41561-019-0461-0

Lyons, J. J., & Waite, G. P. (2011). Dynamics of explosive volcanism at Fuego volcano imaged with very long period seismicity. *Journal of Geophysical Research*, *116*, B09303. https://doi.org/10.1029/2011JB008521

Maeda, Y., & Takeo, M. (2011). Very-long-period pulses at Asama volcano, central Japan, inferred from dense seismic observations. *Geophysical Journal International*, *185*(1), 265–282. https://doi.org/10.1111/j.1365-246X.2011.04938.x

Maeda, Y., Takeo, M., & Ohminato, T. (2011). A waveform inversion including tilt: Method and simple tests. *Geophysical Journal International*, *184*(2), 907–918. https://doi.org/10.1111/j.1365-246X.2010.04892.x

Maeda, Y., Yamanaka, Y., Ito, T., & Horikawa, S. (2021). Machine-learning-based detection of volcano seismicity using the spatial pattern of amplitudes. *Geophysical Journal International*, *225*(1), 416–444. https://doi.org/10.1093/gji/ggaa593

Malfante, M., Dalla Mura, M., Métaxian, J.-P., Mars, J. I., Macedo, O., & Inza, A. (2018). Machine learning for volcano-seismic signals: Challenges and perspectives. *IEEE Signal Processing Magazine*, *35*(2), 20–30. https://doi.org/10.1109/MSP.2017.2779166

Manley, G. F., Pyle, D. M., Mather, T. A., Rodgers, M., Clifton, D. A., Stokell, B. G., et al. (2020). Understanding the timing of eruption end using a machine learning approach to classification of seismic time series. *Journal of Volcanology and Geothermal Research*, *401*, 106917. https://doi.org/10.1016/j.jvolgeores.2020.106917

Matoza, R., & Chouet, B. A. (2010). Subevents of long-period seismicity: Implications for hydrothermal dynamics during the 2004–2008 eruption of Mount St. Helens. *Journal of Geophysical Research*, *115*, B12206. https://doi.org/10.1029/2010JB007839

Matoza, R., Fee, D., Green, D., & Mialle, P. (2019). Volcano infrasound and the international monitoring system. In *Infrasound monitoring for atmospheric studies* (pp. 1023–1077). Springer. https://doi.org/10.1007/978-3-319-75140-5_33

Matoza, R., Fee, D., Green, D. N., Le Pichon, A., Vergoz, J., Haney, M. M., et al. (2018). Local, regional, and remote seismo-acoustic observations of the April 2015 VEI 4 eruption of Calbuco volcano, Chile. *Journal of Geophysical Research: Solid Earth*, *123*, 3814–3827. https://doi.org/10.1002/2017JB015182

Matoza, R. S., Chouet, B. A., Jolly, A. D., Dawson, P. B., Fitzgerald, R. H., Kennedy, B. M., et al. (2022). High-rate very-long-period seismicity at Yasur volcano, Vanuatu: Source mechanism and decoupling from surficial explosions and infrasound. *Geophysical Journal International*, *230*(1), 392–426. https://doi.org/10.1093/gji/ggab533

McKee, K., Smith, C. M., Reath, K., Snee, E., Maher, S., Matoza, R. S., et al. (2021). Evaluating the state-of-the-art in remote volcanic eruption characterization. Part I: Raikoke volcano, Kuril Islands. *Journal of Volcanology and Geothermal Research*, *419*, 107354. https://doi.org/10.1016/j.jvolgeores.2021.107354

Miller, A., Stewart, R., White, R., Luckett, R., Baptie, B., Aspinall, W., et al. (1998). Seismicity associated with dome growth and collapse at the Soufriere Hills Volcano, Montserrat. *Geophysical Research Letters*, *25*(18), 3401–3404. https://doi.org/10.1029/98GL01778

Minson, S. E., Dreger, D. S., Bürgmann, R., Kanamori, H., & Larson, K. M. (2007). Seismically and geodetically determined nondouble-couple source mechanisms from the 2000 Miyakejima volcanic earthquake swarm. *Journal of Geophysical Research*, *112*, B10308. https://doi.org/10.1029/2006JB004847

Miyabuchi, Y., Ikebe, S., & Watanabe, K. (2008). Geological constraints on the 2003–2005 ash emissions from the Nakadake crater lake, Aso Volcano, Japan. *Journal of Volcanology and Geothermal Research*, *178*(2), 169–183. https://doi.org/10.1016/j.jvolgeores.2008.06.025

Nakano, M., Kumagai, H., & Chouet, B. A. (2003). Source mechanism of long-period events at Kusatsu–Shirane Volcano, Japan, inferred from waveform inversion of the effective excitation functions. *Journal of Volcanology and Geothermal Research*, *122*(3–4), 149–164. https://doi.org/10.1016/S0377-0273(02)00499-7

Newhall, C. G., Costa, F., Ratdomopurbo, A., Venezky, D., Widiwijayanti, C., Win, N. T. Z., et al. (2017). WOVOdat—An online, growing library of worldwide volcanic unrest. *Journal of Volcanology and Geothermal Research*, *345*, 184–199. https://doi.org/10.1016/j.jvolgeores.2017.08.003

Nishida, K., Kobayashi, N., & Fukao, Y. (2000). Resonant oscillations between the solid Earth and the atmosphere. *Science*, *287*(5461), 2244–2246. https://doi.org/10.1126/science.287.5461.2244

Nishimura, T., & Iguchi, M. (2011). *Volcanic earthquakes and tremor in Japan* (English ed.). Kyoto University Press; Distributors, USA and Canada, International Specialized Book Services (ISBS).

Niu, J., & Song, T.-R. (2021). Episodic transport of discrete magma batches beneath Aso volcano. *Nature Communications*, *12*(5555), 1–12. https://doi.org/10.1038/s41467-021-25883-y

Niu, J., & Song, T.-R. A. (2020). Real-time and in-situ assessment of conduit permeability through diverse long-period tremors beneath Aso volcano, Japan. *Journal of Volcanology and Geothermal Research*, *401*, 106964. https://doi.org/10.1016/j.jvolgeores.2020.106964

Nooner, S. L., & Chadwick, W. W. (2009). Volcanic inflation measured in the caldera of Axial Seamount: Implications for magma supply and future eruptions. *Geochemistry, Geophysics, Geosystems*, *10*, Q02002. https://doi.org/10.1029/2008GC002315

Ohkura, S., Yoshikawa, S., Inoue, H., Utsugi, M., & Kagiyama, T. (2009). *Leveling in Aso (September–October 2008): Aso research report 2009 (report in Japanese)*.

Ohminato, T. (2006). Characteristics and source modeling of broadband seismic signals associated with the hydrothermal system at Satsuma–Iwojima volcano, Japan. *Journal of Volcanology and Geothermal Research*, *158*(3–4), 467–490. https://doi.org/10.1016/j.jvolgeores.2006.08.004

Ohminato, T., Chouet, B. A., Dawson, P., & Kedar, S. (1998). Waveform inversion of very long period impulsive signals associated with magmatic injection beneath Kilauea volcano, Hawaii. *Journal of Geophysical Research*, *103*(B10), 23839–23862. https://doi.org/10.1029/98JB01122

Ohminato, T., Takeo, M., Kumagai, H., Yamashina, T., Oikawa, J., Koyama, E., et al. (2006). Vulcanian eruptions with dominant single force components observed during the Asama 2004 volcanic activity in Japan. *Earth Planets and Space*, *58*(5), 583–593. https://doi.org/10.1186/BF03351955

Okada, Y. (1992). Internal deformation due to shear and tensile faults in a half-space. *Bulletin of the Seismological Society of America*, *82*(2), 1018–1040. https://doi.org/10.1785/BSSA0820021018

Okada, Y., Kasahara, K., Hori, S., Obara, K., Sekiguchi, S., Fujiwara, H., & Yamamoto, A. (2004). Recent progress of seismic observation networks in Japan—Hi-net, F-net, K-NET and KiK-net. *Earth Planets and Space*, *56*(8), 15–28. https://doi.org/10.1186/BF03353076

Pallister, J., & McNutt, S. R. (2015). Synthesis of volcano monitoring. In *The encyclopedia of volcanoes* (pp. 1151–1171). Elsevier. https://doi.org/10.1016/b978-0-12-385938-9.00066-3

Park, I., Jolly, A., Lokmer, I., & Kennedy, B. (2020). Classification of long-term very long period (VLP) volcanic earthquakes at Whakaari/White Island volcano, New Zealand. *Earth Planets and Space*, *72*(1), 1–10. https://doi.org/10.1186/s40623-020-01224-z

Pinel, V., Poland, M. P., & Hooper, A. (2014). Volcanology: Lessons learned from synthetic aperture radar imagery. *Journal of Volcanology and Geothermal Research*, *289*, 81–113. https://doi.org/10.1016/j.jvolgeores.2014.10.010

Poland, M. (2015). Volcano monitoring from space. In S. C. Loughlin, R. S. J. Sparks, S. K. Brown, S. F. Jenkins, & C. Vye-Brown (Eds.), *Global volcanic hazards and risk* (pp. 311–316). U.S. Gelogical Society. https://doi.org/10.1017/cbo9781316276273.019

Prejean, S. G., & Brodsky, E. E. (2011). Volcanic plume height measured by seismic waves based on a mechanical model. *Journal of Geophysical Research*, *116*, B01306. https://doi.org/10.1029/2010JB007620

Pritchard, M. E., Mather, T., McNutt, S. R., Delgado, F., & Reath, K. (2019). Thoughts on the criteria to determine the origin of volcanic unrest as magmatic or non-magmatic. *Philosophical Transactions of the Royal Society A*, *377*(2139), 20180008. https://doi.org/10.1098/rsta.2018.0008

Pritchard, M. E., & Simons, M. (2002). A satellite geodetic survey of large-scale deformation of volcanic centres in the central Andes. *Nature*, *418*(6894), 167–171. https://doi.org/10.1038/nature00872

Reath, K., Pritchard, M., Poland, M., Delgado, F., Carn, S., Coppola, D., et al. (2019). Thermal, deformation, and degassing remote sensing time series (CE 2000–2017) at the 47 most active volcanoes in Latin America: Implications for volcanic systems. *Journal of Geophysical Research: Solid Earth*, *124*, 195–218. https://doi.org/10.1029/2018JB016199

Richardson, J. P., & Waite, G. P. (2013). Waveform inversion of shallow repetitive long period events at Villarrica Volcano, Chile. *Journal of Geophysical Research: Solid Earth*, *118*, 4922–4936. https://doi.org/10.1002/jgrb.50354

Rowe, C. A., Aster, R. C., Kyle, P. R., Schlue, J. W., & Dibble, R. R. (1998). Broadband recording of Strombolian explosions and associated very-long-period seismic signals on mount Erebus volcano, Ross Island, Antarctica. *Geophysical Research Letters*, *25*(13), 2297–2300. https://doi.org/10.1029/98GL01622

Ruppert, N. A., Prejean, S., & Hansen, R. A. (2011). Seismic swarm associated with the 2008 eruption of Kasatochi Volcano, Alaska: Earthquake locations and source parameters. *Journal of Geophysical Research*, *116*, B00B07. https://doi.org/10.1029/2010JB007435

Saito, G., Ishizuka, O., Ishizuka, Y., Hoshizumi, H., & Miyagi, I. (2018). Petrological characteristics and volatile content of magma of the 1979, 1989, and 2014 eruptions of Nakadake, Aso volcano, Japan. *Earth Planets and Space*, *70*(1), 197. https://doi.org/10.1186/s40623-018-0970-x

Sakaguchi, H., Sudo, Y., Sawada, Y., & Yoshikawa, S. (2008). Relationship between the explosive activities and the associated volcanic tremors observed at Nakadake summit of Aso volcano—The temporal variation in amplitude of tremors recorded by Wiechert seismograph (in Japanese). *Bulletin of the Volcanological Society of Japan*, *53*, 143–149.

Sandanbata, O., Kanamori, H., Rivera, L., Zhan, Z., Watada, S., & Satake, K. (2021). Moment tensors of Ring-faulting at active volcanoes: Insights into vertical-CLVD earthquakes at the Sierra Negra caldera, Galápagos islands. *Journal of Geophysical Research: Solid Earth*, *126*, e2021JB021693. https://doi.org/10.1029/2021JB021693

Sandanbata, O., Obara, K., Maeda, T., Takagi, R., & Satake, K. (2015). Sudden changes in the amplitude-frequency distribution of long-period tremors at Aso volcano, southwest Japan: Sudden changes in long-period volcanic tremors. *Geophysical Research Letters*, *42*, 10256–10262. https://doi.org/10.1002/2015GL066443

Sassa, K. (1935). *Geophysical studies on the volcano Aso. (Part 1: Volcanic micro-tremors and eruptive-earthquakes). Memoirs of the College of Science, Kyoto Imperial University. Series A* (pp. 255–293).

Sassa, K. (1936). *Micro-seismometrical study on eruptions of the volcano Aso (Part II, of the geophysical studies on the volcano Aso). Memoirs of the College of Science, Kyoto Imperial University*.

Schlindwein, V., Müller, C., & Jokat, W. (2005). Seismoacoustic evidence for volcanic activity on the ultraslow-spreading Gakkel ridge, Arctic ocean. *Geophysical Research Letters*, *32*, L18306. https://doi.org/10.1029/2005GL023767

Schmid, F., Schlindwein, V., Koulakov, I., Plötz, A., & Scholz, J.-R. (2017). Magma plumbing system and seismicity of an active mid-ocean ridge volcano. *Scientific Reports*, *7*(1), 1–9. https://doi.org/10.1038/srep42949

Shapiro, N. M., Ritzwoller, M., & Bensen, G. (2006). Source location of the 26 sec microseism from cross-correlations of ambient seismic noise. *Geophysical Research Letters*, *33*, L18310. https://doi.org/10.1029/2006GL027010

Shuler, A., Nettles, M., & Ekström, G. (2013). Global observation of vertical-CLVD earthquakes at active volcanoes. *Journal of Geophysical Research: Solid Earth*, *118*, 138–164. https://doi.org/10.1029/2012JB009721

Smithsonian Institution, & Venzke, G. (2013). Volcanoes of the World, v. 4.3.4 [Dataset]. Global Volcanism Program. https://doi.org/10.5479/si.GVP.VOTW4-2013

Sparks, R., Annen, C., Blundy, J., Cashman, K., Rust, A., & Jackson, M. (2019). Formation and dynamics of magma reservoirs. *Philosophical Transactions of the Royal Society A*, *377*(2139), 20180019. https://doi.org/10.1098/rsta.2018.0019

Sparks, R., Biggs, J., & Neuberg, J. (2012). Monitoring volcanoes. *Science*, *335*(6074), 1310–1311. https://doi.org/10.1126/science.1219485

Sudo, Y., & Kong, L. (2001). Three-dimensional seismic velocity structure beneath Aso volcano, Kyushu, Japan. *Bulletin of Volcanology*, *63*(5), 326–344. https://doi.org/10.1007/s004450100145

Sudo, Y., Tsutsui, T., & Nakaboh, M. (2006). Ground deformation and magma reservoir at Aso volcano: Location of deflation source derived from long-term geodetic surveys (in Japanese). *Bulletin of the Volcanological Society of Japan*, *51*, 291–309.

Takei, Y., & Kumazawa, M. (1994). Why have the single force and torque been excluded from seismic source models? *Geophysical Journal International*, *118*(1), 20–30. https://doi.org/10.1111/j.1365-246x.1994.tb04672.x

Takei, Y., & Kumazawa, M. (1995). Phenomenological representation and kinematics of general seismic sources including the seismic vector modes. *Geophysical Journal International*, *121*(3), 641–662. https://doi.org/10.1111/j.1365-246x.1995.tb06428.x

Takeo, M., Yamasato, H., Furaya, I., & Seino, M. (1990). Analysis of long-period seismic waves excited by the November 1987 eruption of Izu-Oshima volcano. *Journal of Geophysical Research*, *95*(B12), 19377–19393. https://doi.org/10.1029/JB095iB12p19377

Tanada, T., Ueda, H., Nagai, M., & Ukawa, M. (2017). NIED's V-net, the fundamental volcano observation network in Japan. *Journal of Disaster Research*, *12*(5), 926–931. https://doi.org/10.20965/jdr.2017.p0926

Tepp, G., Dziak, R. P., Haney, M. M., Lyons, J. J., Searcy, C., Matsumoto, H., & Haxel, J. (2020). Seismic and hydroacoustic observations of the 2016–17 Bogoslof eruption. *Bulletin of Volcanology*, *82*(1), 1–21. https://doi.org/10.1007/s00445-019-1344-3

Tilling, R. (2008). The critical role of volcano monitoring in risk reduction. *Advances in Geosciences*, *14*, 3–11. https://doi.org/10.5194/adgeo-14-3-2008

Titos, M., Bueno, A., Garcia, L., & Benitez, C. (2018). A deep neural networks approach to automatic recognition systems for volcano-seismic events. *IEEE Journal of Selected Topics in Applied Earth Observations and Remote Sensing*, *11*(5), 1533–1544. https://doi.org/10.1109/JSTARS.2018.2803198

Tolstoy, M., Bohnenstiehl, D., Edwards, M., & Kurras, G. (2001). Seismic character of volcanic activity at the ultraslow-spreading Gakkel Ridge. *Geology*, *29*(12), 1139–1142. https://doi.org/10.1130/0091-7613(2001)029<1139:SCOVAA>2.0.CO;2

Tolstoy, M., Cowen, J., Baker, E., Fornari, D., Rubin, K., Shank, T., et al. (2006). A sea-floor spreading event captured by seismometers. *Science*, *314*(5807), 1920–1922. https://doi.org/10.1126/science.1133950

Uhira, K., & Takeo, M. (1994). The source of explosive eruptions of Sakurajima volcano, Japan. *Journal of Geophysical Research*, *99*(B9), 17775–17789. https://doi.org/10.1029/94JB00990

Ukawa, M., & Ohtake, M. (1987). A monochromatic earthquake suggesting deep-seated magmatic activity beneath the Izu-Ooshima Volcano, Japan. *Journal of Geophysical Research*, *92*(B12), 12649–12663. https://doi.org/10.1029/JB092iB12p12649

van Driel, M., Wassermann, J., Pelties, C., Schiemenz, A., & Igel, H. (2015). Tilt effects on moment tensor inversion in the near field of active volcanoes. *Geophysical Journal International*, *202*(3), 1711–1721. https://doi.org/10.1093/gji/ggv209

Varley, N., Arámbula-Mendoza, R., Reyes-Dávila, G., Sanderson, R., & Stevenson, J. (2010). Generation of Vulcanian activity and long-period seismicity at Volcán de Colima, Mexico. *Journal of Volcanology and Geothermal Research*, *198*(1–2), 45–56. https://doi.org/10.1016/j.jvolgeores.2010.08.009

Waite, G. P., Chouet, B. A., & Dawson, P. B. (2008). Eruption dynamics at Mount St. Helens imaged from broadband seismic waveforms: Interaction of the shallow magmatic and hydrothermal systems. *Journal of Geophysical Research*, *113*, B02305. https://doi.org/10.1029/2007JB005259

Waite, G. P., Nadeau, P. A., & Lyons, J. J. (2013). Variability in eruption style and associated very long period events at Fuego volcano, Guatemala. *Journal of Geophysical Research: Solid Earth*, *118*, 1526–1533. https://doi.org/10.1002/jgrb.50075

Watada, S., & Kanamori, H. (2010). Acoustic resonant oscillations between the atmosphere and the solid Earth during the 1991 Mt. Pinatubo eruption. *Journal of Geophysical Research*, *115*, B12319. https://doi.org/10.1029/2010JB007747

Watts, A., Peirce, C., Grevemeyer, I., Paulatto, M., Stratford, W., Bassett, D., et al. (2012). Rapid rates of growth and collapse of Monowai submarine volcano in the Kermadec Arc. *Nature Geoscience*, *5*(7), 510–515. https://doi.org/10.1038/ngeo1473

Wech, A., Tepp, G., Lyons, J., & Haney, M. (2018). Using earthquakes, T waves, and infrasound to investigate the eruption of Bogoslof volcano, Alaska. *Geophysical Research Letters*, *45*, 6918–6925. https://doi.org/10.1029/2018GL078457

Widmer, R., & Zürn, W. (1992). Bichromatic excitation of long-period Rayleigh and air waves by the Mount Pinatubo and El Chichon volcanic eruptions. *Geophysical Research Letters*, *19*(8), 765–768. https://doi.org/10.1029/92GL00685

Wilcock, W. S., Tolstoy, M., Waldhauser, F., Garcia, C., Tan, Y. J., Bohnenstiehl, D. R., et al. (2016). Seismic constraints on caldera dynamics from the 2015 Axial Seamount eruption. *Science*, *354*(6318), 1395–1399. https://doi.org/10.1126/science.aah5563

Williams, C. A., & Wadge, G. (1998). The effects of topography on magma chamber deformation models: Application to Mt. Etna and radar interferometry. *Geophysical Research Letters*, *25*(10), 1549–1552. https://doi.org/10.1029/98GL01136

Woods, J., Donaldson, C., White, R. S., Caudron, C., Brandsdóttir, B., Hudson, T. S., & Ágústsdóttir, T. (2018). Long-period seismicity reveals magma pathways above a laterally propagating dyke during the 2014–15 Bárðarbunga rifting event, Iceland. *Earth and Planetary Science Letters*, *490*, 216–229. https://doi.org/10.1016/j.epsl.2018.03.020

Wright, I. C., Chadwick, W. W., Jr., de Ronde, C. E., Reymond, D., Hyvernaud, O., Gennerich, H.-H., et al. (2008). Collapse and reconstruction of Monowai submarine volcano, Kermadec arc, 1998–2004. *Journal of Geophysical Research*, *113*, B08S03. https://doi.org/10.1029/2007JB005138

Xia, Y., & Chen, X. (2020). Observation of a new long-period (16-s) persistent tremor originating in the Gulf of Guinea. *Geophysical Research Letters*, *47*, e2020GL088137. https://doi.org/10.1029/2020GL088137

Xia, Y., Ni, S., & Zeng, X. (2013). Twin enigmatic microseismic sources in the Gulf of Guinea observed on intercontinental seismic stations. *Geophysical Journal International*, *194*(1), 362–366. https://doi.org/10.1093/gji/ggt076

Yamamoto, M. (2005). *Volcanic fluid system Inferred from broadband seismic signals* (PhD dissertation). University of Tokyo.

Yamamoto, M., Kawakatsu, H., Kaneshima, S., Mori, T., Tsutsui, T., Sudo, Y., & Morita, Y. (1999). Detection of a crack-like conduit beneath the active crater at Aso volcano Japan. *Geophysical Research Letters*, *26*(24), 3677–3680. https://doi.org/10.1029/1999GL005395

Yamamoto, M., Kawakatsu, H., Yomogida, K., & Koyama, J. (2002). Long-period (12 sec) volcanic tremor observed at Usu 2000 eruption: Seismological detection of a deep magma plumbing system. *Geophysical Research Letters*, *29*(9), 43-1–43-4. https://doi.org/10.1029/2001GL013996

Yamasato, H., Yokota, T., & Kashiwabara, S. (1991). Earthquake swarm and volcanic tremors off eastern Izu Peninsula in 1989. *Journal of Physics of the Earth*, *39*(1), 79–92. https://doi.org/10.4294/jpe1952.39.79

Ye, L., Kanamori, H., Rivera, L., Lay, T., Zhou, Y., Sianipar, D., & Satake, K. (2020). The 22 December 2018 tsunami from flank collapse of Anak Krakatau volcano during eruption. *Science Advances*, *6*(3), eaaz1377. https://doi.org/10.1126/sciadv.aaz1377

Zeng, X., & Ni, S. (2010). A persistent localized microseismic source near the Kyushu Island, Japan. *Geophysical Research Letters*, *37*, L24307. https://doi.org/10.1029/2010GL045774

Zeng, X., & Ni, S. (2014). Evidence for an independent 26-s microseismic source near the Vanuatu Islands. *Pure and Applied Geophysics*, *171*(9), 2155–2163. https://doi.org/10.1007/s00024-014-0811-1

Zhu, L. (2003). Recovering permanent displacements from seismic records of the June 9, 1994 Bolivia deep earthquake. *Geophysical Research Letters*, *30*(14), 1740. https://doi.org/10.1029/2003GL017302

Zhu, L., & Rivera, L. A. (2002). A note on the dynamic and static displacements from a point source in multilayered media: A note on the dynamic and static displacements from a point source. *Geophysical Journal International*, *148*(3), 619–627. https://doi.org/10.1046/j.1365-246X.2002.01610.x